acp-2018-1162
Author Response to Referee Comments

We thank the three referees for their very useful comments. Please find below our responses. These are followed by a revised version of our manuscript, with all changes marked.

Referee #1 (acp-2018-1162-RC1)

This manuscript describes a new soon-to-be-launched Swedish satellite mission. This mission will combine UV (for NLC) and IR (for the O2 (0,0) airglow emission band) limb observations with IR nadir imaging, to study the dynamics of the upper atmosphere, specifically gravity waves. This paper gives an overview of the scientific background and objectives, then it describes the instrument design and several analysis techniques, before explaining the operating modes and summarizing the mission.

It is somehow unusual to comment on a paper giving an overview of a project which has probably been extensively reviewed before getting funded by the Swedish National Space Agency. I assume that most of the possible issues have been investigated already, so my comments will be more about lacking information, even if I understand that a simple paper cannot cover all the technical details involved in such a mission, and some personal remarks.

How can the second scientific question be answered since there is no thermospheric measurements above ~96 km, no ionospheric measurements or modeling involved in MATS? Does it depends on external collaborations?

Yes, the connection to the ionospheric questions relies on collaboration with other missions and databases. Similarly, the connections to the lower atmosphere (first science question) will rely on external such collaborations. This is stated in the paragraph following the science questions, and some examples of collaborations are given in Section 6 (Outlook).

I don’t understand some of the instruments parameters. For example, Tables 5 and 6 gives 10x10 km for the nadir resolution. In section 3.4, it is said that the fov will be 200x50 km, and in section 3.2.4, that the CDD format is 512x2048 px, therefore the spatial resolution should be 100x100 m. Is there any binning involved? How much? Or will the images be cropped?

In all channels, information from the individual CCD pixels will be binned into larger image pixels (during usual scientific operation as listed in Table 5 and 6). This is required in order not to exceed the data rate available from the satellite downlink. The caption of the tables clarifies that information given in the tables refers to binned image pixels. For the nadir channel, binning into 10x10 km image pixels is performed. Sampling with larger resolution would not be meaningful because of the nadir image smearing (along track) due to the satellite motion.

The authors should give the speed of the satellite, it is important to understand the effects due to smearing. The readout times are close to the exposure times (tables 5 and 6), and up to 5s, which seem rather large for a satellite moving at probably several km/s. 4.2.2 briefly mentions readout smearing but doesn’t give much information or references about desmearing. It also doesn’t give any errors on the GW parameters measurements due to this effect.

The different kinds of smearing are described in the manuscript:

In section 3.2.4, we refer to readout smearing during the CCD readout (row-shifting). The handling of this CCD readout smearing is discussed further in section 4.2.2.

At the end of section 2.2 and in section 3.4, we refer to smearing of the nadir images due to the satellite motion ("motion blur"). We have now added information about the satellite speed (~7 km s^{-1}*) in section 3.4. Methods for compensating for motion smearing exist in terms of synchronized CCD row shifting ("push broom technique"), but are not applicable to the MATS nadir imager. The only measure against motion blur applied in the MATS nadir channel is a restriction of the exposure time to max 1 s. Together with the readout resolution of the nadir images (10x10 km), this results in a spatial resolution of about 15 km along track. For the limb channels, on the other hand, retrieval simulations show that motion blur is not a significant limitation for the spatial resolution achievable by the tomography. The satellite moves up to 35 km during image exposure, but this is still much shorter than the e.g. the 700 km limb line-of-sight through a 10 km thick airglow layer.*

Table 1 shows the expected measurement precisions. 5-20 K for the O2 nighttime temperature is very large given that this range will correspond to the temperature perturbations expected for the most impactful GWs.

Indeed, the spectral analysis of the temperature works best during daytime when the O2 dayglow provides the best signal-to-noise ratio for Atmospheric Band temperature retrieval and tomographic wave analysis. At nighttime, the precision of the nightglow O2 Atmospheric Band temperature retrieval is limited. When providing temperature data with the maximum tomographic resolution of 60x20x1 km, the precision of the temperature will not be better than 5-20 K (Table 1). The temperature precision can be improved by spatial averaging (either in terms of image pixel binning or in terms of post-flight data processing), which of course will diminish the spatial resolution. However this trade-off is handled, the possibilities to obtain small scale gravity wave data from the temperature field are rather limited during nighttime. We have now added text in section 4.5 stating this more clearly. Nonetheless, good nighttime gravity wave data is expected from other retrieved data fields (nightglow volume emission rate, atomic oxygen).

What will be the error on momentum flux calculation?

The ability to derive momentum flux depends on observation condition and the spectral sensitivity of the wave retrieval to different horizontal and vertical wavelength. A detailed discussion of the possibilities and limitation of retrieving different wave properties is beyond the scope of the present manuscript and will be provided as part of future wave studies. In the current manuscript, we have moved our description of the wave retrieval to a new, separate section 4.7, and extended it with a basic account of the steps involved in the planned wave analysis.

The satellite will fly on a sunsynchronous, near-terminator, polar orbit, which means it will be complicated to look at tidal effects.

Yes, possibilities to infer tidal information from the MATS data will be very limited. At a given latitude, data will be obtained at two (rather) fixed local times only. This fact actually facilitates our efforts to obtain a consistent gravity wave climatology. Since the gravity wave *analysis is performed in a fixed phase of the (migrating) tide, variations due to tidal influences are minimized in our data set. A deeper analysis of relationships between gravity waves and tides will require co-analysis with external data sets.*

Several corrections rely on climatologies or models. Is it planned to improved the corrections in the future?

With a "low-budget" mission like MATS it has not been possible to design a completely self-sustained system that can provide all information necessary from in-orbit measurements, on-board calibration etc. We thus need to rely on external data, climatologies, and simulations to obtain a complete set of information that is necessary for the data analysis.

An example is knowledge about the atmospheric density (or pressure) profile that is necessary e.g. for the retrieval of certain wave parameters or for the subtraction of molecular scattering background from the NLC measurements. There are ideas to use measurements of Rayleigh scattering in several channels to retrieve limited density information. However, such approaches are difficult to quantify before actual flight data become available, and we thus do not want to speculate in the manuscript about other possibilities than using climatologies or model atmospheres as a source for atmospheric density.

Figure 9 shows the sensitivity to GW horizontal and vertical wavelengths for the limb instrument. The best "region" is for 3 < Lz < 10 km and Lh > ~60 km. These waves won't be observable by the nadir instrument because of the integration through the O2 layer. How do you plan to combine limb and nadir results?

As we state in the manuscript, possibilities are limited to obtain useful data from the nadir channel and to combine these data with the limb analysis. The nadir observations concern O2 nightglow and require sufficient darkness (large solar zenith angles) in order to provide useful data. The near-terminator orbit chosen for MATS is not optimized for these nadir observations and will provide sufficient darkness largely only during high-latitude winter conditions. The tomographic limb analysis, on the other hand, works best during daytime when O2 dayglow provides the best signal-to-noise ratio for temperature retrieval and tomographic wave analysis. At nighttime, the precision of the nightglow O2 Atmospheric Band temperature retrieval is limited (Table 1), requiring spatial averaging and thus prohibiting wave analysis down to the small horizontal scales accessible in daytime. (We have added more text in Section 4.5 to clarify this. See also our response above to the reviewer's question about the O2 nighttime temperature) The possibilities for combined wave analysis from nadir and limb observations are therefore rather limited during this mission. In this sense, the addition of the nadir imager may be regarded as an interesting test of an observational concept rather than an essential part of this mission. Nonetheless, we do expect exciting case studies with detailed nadir observations of wave events in the O2 Atmospheric Band nightglow, in combination with limb analysis of atmospheric background conditions in terms of temperature and odd oxygen fields.

Furthermore, a large part of the important GWs (the ones transporting a lot of momentum) will be poorly characterized, especially GWs with Lh < 60 km. What is the expected impact on the GW and MF climatology? I understand some of these questions/comments may be out of the scope of this paper, but it would be interesting to provide some answers or clarifications.

Figure 9 in the original manuscript (now Figure 11 in the revised manuscript) only shows the retrieval sensitivity for waves with wave fronts perpendicular to the orbit plane. As described in the text, because of the higher retrieval resolution across track, waves with wave fronts parallel to the orbit plane can be inferred with horizontal wavelengths down to 20 km. This asymmetry in the retrieval resolution between along track and across track is a complication for our data analysis. However, it means that in most cases, waves with horizontal wavelengths well below 60 km can be identified. This is true in particular since gravity waves tend to travel (anti)parallel to the mean wind, i.e. preferably in east-west direction, and thus with their wave fronts oriented parallel to the orbit plane (close to north-south for most of the orbit). In the extended Section 4.7, we briefly describe the need to specify a "sensitivity function" that defines the response of our retrievals in terms of a wave's wavelength and orientation as well as observation conditions. This is necessary for a proper analysis of gravity wave and momentum flux spectra. A deeper discussion is indeed beyond the scope of the current overview paper.

Minor edits

The minor edits listed below have been corrected. We apologize for leaving so many misspellings and stylistic errors in the manuscripts, and we thank the reviewer for a thorough work in identifying those.

p3 l.11: Ern et al., 2011
p4 l.16: first sentence sounds weird
p4 l.20: Forbes et al., 2009
p4 l.23: Funke et al., 2010
p4 l.30: ...satellite measurements...
p5 l.4: could include Azeem et al., 2015
p5 l.13: Gong et al., 2012
p5 l.15: combining
p6 l.3: by Song et al.
p6 l.25: remove "in"
p7 l.4-6: looks like there is only 1 science question concerning NLC
p8 l.6: Sheese et al., 2010
p8 l.9: Mlynczack et al., 2001
p8 l.11: patterns
p8 l.13: von Savigny et al., 2005
p9 l.13-14: change [] to () for the references
p9 l.21: Llewellyn
p15 l.12: line stops too early, maybe pdf issue
p16 l.17: analog-to-digital
p16 l.22: section 0???
p17 l.12: ...is better than...
p17 l.17: Figure 6 shows...
p21 l.7: field of view
p22 l.14: a priori... a posteriori
p22 l.31: 175 km
p23 l.5: a priori
p23 l.8: change +- to normal sign
p26 l.1: in terms of...

p26 l.3: excited
p26 l.9: provide
p26 l.21: retrievals
p26 l.31: ratio
p28 l.19: MATS

Referee #2 **(acp-2018-1162-RC2)**

This paper is an overview of the new Swedish satellite mission, MATS, which will be launched in 2019. It is thoroughly written, covering scientific objectives, instrumentations, retrieval methods for tomography, etc. No major concerns were found. Only some minor issues. Publication in the ACP LPMR special issue is recommended after some clarifications being made.

Some references cannot be found in the reference list.
The reference has been checked and some references have been added.

Comments:

1. Page 1, line 16, “gravity wave interactions”, interactions with what? And many places throughout the manuscript.
We usually refer to gravity wave interactions both with larger scale waves and with the mean flow. This has now been added explicitly in some (but not all) places.

2 Abstract, “Major scientific objectives…”. This sentence is redundant with the first sentence in the abstract.
We have changed this. The first sentence is now a general statement, while the latter is about the wave interactions (see above).

3. Page 2, line 1, “large scale circulation” -à”large scale circulations”
Corrected.

4. page 2, line 5, “upwell at the summer pole”, the summer polar region might be a better expression. Same to “ the winter pole”.
Corrected.

5. page 2, line 9, nomenclature, why “PMCs” are not used in this paper? Aren’t PMCs often used by satellite measurements?
Some scientists indeed talk about PMC when observing from satellites, and NLC when observing in other ways. But it is the same thing, and there is no general rule. The MATS project very much builds on the heritage of Georg Witt, and in his spirit we stick to the nomenclature NLC.

6. page 2, line 22, “is today understood”, is there a typo?
We have clarified the statement by moving "today" to an earlier part of the sentence.

7. page 2, line 23, “important mechanisms and interactions”, what mechanisms and interactions? Please specify.

This is now specified in the subsequent sentences about wave sources, dissipation and forcing, with momentum flux as the decisive quantity.

8. page 3, line 6, “MLT data…”, gravity wave observations in the MLT?
This has been adopted.

9. page 3, line 14, “Also concerning mesospheric ice formation and NLC..”, this sentence jumped out of nowhere in a gravity wave paragraph. How about a separate paragraph on the importance of NLC studies?
This is a good suggestion. We have done so.

10. page 5, line 9, “extending below 100 km” and “extending below 10 km”, this could cause some confusion. “Below 100 km” means below 100 km altitude? How about “extending shorter than 100 km wavelength”?
This is done.

11. page 5, line 21, “NLC” should use plural. “NLCs”
Corrected.

12. page 7, line 16, “Both O atmospheric band airglow and NLC feature…”. It is very difficult to convert gravity waves in NLCs to temperature, geopotential or wind perturbations of gravity waves, that could be useful for models. Can the authors comment on this?
We state "Both O2 Atmospheric Band airglow and NLC feature horizontal and vertical structures that are a direct response to gravity wave activity." This does not mean that vertical structures in NLC can be used to retrieve vertical gravity wave properties. On the contrary, the wave analysis of NLC data will be restricted to horizontal wave structures. This is described later in this Section 2.2.

13. Figure 1. What are the red and purple lines in the two boxes?
The lines represent limb lines of sight through a given volume for an Atmospheric Band channel and an NLC channel, respectively. This is now explained more clearly in the figure caption.

14. page 8, line 11, “patters” or “patterns”?
Corrected.

15. page 9, lines 8-10, “nadir” actually means “from below the satellite.
Yes. Still, it makes sense to state this explicitly in this introductory sentence about the nadir imager.

16. page 9, the paragraph below Table 1. The orbit is near terminator (sunrise or sunset). Are you sure the nadir imager can see nightglow?
Indeed, sufficiently dark nadir measurement conditions will be restricted to the winter season at mid and high latitudes, i.e. a minor part of the total mission. This is now more clearly stated in this paragraph.

17. page 15, line 12, “Since the MATS…”, this sentence belongs to the paragraph below.
Corrected.

18. page 16, line 22, “Section 0”?
Corrected.

19. page 17, line 17, “Figure..” which figure?
Corrected.

20. page 21, line 26, “MSIS-90”, a newer version of MSIS is available: https://en.wikipedia.org/wiki/NRLMSISE-00. Why chose to use an older version of MSIS?
We have now updated this. The use of MSIS-90 was a heritage from the NLC analysis of the Odin satellite mission.

Referee #3 (acp-2018-1162-RC3)

This manuscript describes a new Swedish satellite mission to study gravity waves in the MLT region by tomographic techniques, applied to airglow emission spectroscopy and scattered sunlight from NLC. This mission provides the possibility of imaging gravity waves in 3-D on a global basis, and has the potential to provide much-needed input to global models which currently rely on parameterization methods. This paper is well written and lays out all technical and scientific aspects of the mission. I recommend publication after making minor revisions.

The most important issue that I found lacking was that of handling the issue of polarization. Polarized light will undergo different effects depending upon the angle of incidence on metallic mirrors. In fact, on reflection circularly-polarization light will likely be produced. It is well-known that sunlight is highly polarized, so that any instrument that responds differently, based on the geometry, will be affected, and unless these effects are handled during calibration, would have significant effects on the received signal. Only once was the word polarization used. I am sure the authors are well aware of this effect, and am puzzled why this was not discussed in their paper.

As the referee states, polarisation will have an impact on the received signal. Some text has been added to highlight this in section 4.3. Based on pre-flight analysis, a main cause of polarisation response in the MATS instrument are the beamsplitters mounted at 45 degree to the incoming beam. At this moment of writing, the laboratory analysis of the instrument's polarization sensitivity is still ongoing as part of the calibration and characterisation procedures.

Different contributions to the total detected signal in orbit (airglow emission, NLC scattering, molecular scattering, including scattering of both direct sunlight and upwelling radiation) have different polarisation properties. As these contributions cannot be separated from each other based on the in-orbit measurements alone, assumptions need to be made during the radiometric calibration of the images. For the different measurement channels the following assumptions will be made:

1. UV: Single scattering will be assumed both for the light scattered of NLCs and the background Rayleigh scattering. This can be assumed as upwelling radiation from the lower atmosphere in the UV to a large extent is absorbed by the ozone layer.

2. IR: In the O2 Atmospheric band region the scattering geometry is different. For the airglow emission unpolarised radiation can be assumed but for the scattered background radiation it is more complex. We have carried out an analysis using the SASKTRAN radiative transfer simulator to estimate the variability in polarisation of the scattered background. These simulations indicate that the background polarisation ratio will vary from between 0.1 to 0.2 depending on the albedo of the lower atmosphere. These differences are negligible at the peak altitudes of the A-band emission, but will have a significant impact on the temperature retrieval (>5 K) at the lower and upper boundaries. However, it is expected that this uncertainty can be reduced by utilizing data from the albedo photometers to quantify the contribution of upwelling radiation to the scattered background radiation.

Other editing comments:

Before line 15: relevant “to” (the last word is missing)
Corrected.

Line 12 add the word “been” in between the words “have” and “retrieved”
Corrected.

Line 15: “combing”-> “combining”
Corrected.

Line 26: “limb imaging also opens”. Better to say “limb imaging also provides”
Corrected.

Line 10, new section: “patters-> “patterns”
Corrected.

Page 26, last sentence” “ration”-> “ratio” The axial ratio used by Lumpe et al in the T-matrix formulation of scattering was assumed to be 2, not 0.5.: from Lumpe et al: “The particles are assumed to be oblate spheroids with an axial ratio of 2”
Yes, this is correct. We have been aware that the CIPS retrieval assumes oblate spheroids, but we have misinterpreted the axial ratio and referred to its inverse in our manuscript. This has now been corrected.

“explicitly simulate of GW’s -omit the word “of”
Corrected.

Gravity waves have also been extracted from AIM SOFIE data (not in NLC), and are discussed in various references, e.g. the following: Gao, H., G. G. Shepherd, Y. Tang, L. Bu, Z. Wang (2017), Double-layer structure in polar mesospheric clouds observed from SOFIE/AIM, Ann. Geophys, 35, 295-309, doi:10.5194/angeo-35-295-2017.
We missed out on this gravity wave data product from SOFIE. We have now added it to the manuscript.

Other:

Sections 4.2 (calibration) and 4.3 (background removal) have undergone some rewriting. This comprises a discussion of polarization (in response to Referee #3) but also other improvements.

The description of gravity wave retrievals has been extended and moved from section 4.4.3 to the new section 4.7. This provides a more logical structure to the overall description of the data analysis (first tomography, then spectroscopy, then wave retrieval), and also follows the reviewers' questions about the planned wave analysis.

Some new references have been added:

Azeem, I., Yue, J., Hoffmann, L., Miller, S. D., Straka III, W. C., and Crowley, G.: Multisensor profiling of a concentric gravity wave event propagating from the troposphere to the ionosphere, Geophys. Res. Lett., 42, 7874-7880, doi: 10.1002/2015GL065903, 2015.

Christensen O. M., Eriksson, P., Urban, Murtagh, D. P., Hultgren, K., and Gumbel, J.: Tomographic retrieval of water vapour and temperature around polar mesospheric clouds using Odin-SMR, Atmos. Meas. Tech., 8, 1981-1999, doi: 10.5194/amt-8-1981-2015, 2015.

Hammar, A., Park, W., Chang, S., Pak, S., Emrich, A., and Stake, J.: Wide-field off-axis telescope for the Mesospheric Airglow/Aerosol Tomography Spectroscopy satellite, Appl. Opt. 58, 1393-1399, doi: 10.1364/AO.58.001393, 2019.

Kaifler, N., Kaifler, B., Wilms, H., Rapp, M., Stober, G., and Jacobi, C.: Mesospheric temperature during the extreme midlatitude noctilucent cloud event on 18/19 July 2016. J. Geophys. Res., 123, 13775–13789, doi: 10.1029/2018JD029717, 2018.

Liu,X., Yue, J., Xu, J., Wang, L., Yuan, W., Russell III, J. M., and Hervig, M. E.: Gravity wave variations in the polar stratosphere and mesosphere from SOFIE/AIM temperature observations, J. Geophys. Res., 119, 7368-7381, doi: 10.1002/2013JD021439, 2014.

Rapp, M., Lübken, F.-J., Müllemann, A., Thomas, G. E., and Jensen, E. J.: Small-scale temperature variations in the vicinity of NLC: Experimental and model results, J. Geophys. Res., 107 (D19), 4392, doi: 10.1029/2001JD001241, 2002.

The MATS Satellite Mission – Gravity Waves Studies by Mesospheric Airglow/Aerosol Tomography and Spectroscopy

Jörg Gumbel[1], Linda Megner[1], Ole Martin Christensen[1,2], Seunghyuk Chang[3], Joachim Dillner[1], Terese Ekebrand[4], Gabriel Giono[5], Arvid Hammar[4,6], Jonas Hedin[1], Nickolay Ivchenko[5,7], Bodil Karlsson[1], Mikael Kruse~~e~~[4], Anqi Li[2], Steven McCallion[4], Donal P. Murtagh[2], Georgi Olentšenko[5], Soojong Pak[8], Woojin Park[8], Jordan Rouse[4], Jacek Stegman[1], Georg Witt[1]

[1]Department of Meteorology (MISU), Stockholm University, Stockholm, Sweden
[2]Earth and Space Sciences, Chalmers University of Technology, Göteborg, Sweden
[3]Center for Integrated Smart Sensors, KAIST Dogok Campus, Seoul, Republic of Korea
[4]Omnisys Instruments AB, August Barks gata 6B, Västra Frölunda, Sweden
[5]School of Electrical Engineering, Royal Institute of Technology (KTH), Stockholm, Sweden
[6]Department of Microtechnology and Nanoscience, Chalmers University of Technology, Göteborg, Sweden
[7]South African National Space Agency, Hermanus 7200, South Africa
[8]School of Space Research, Kyung Hee University, Yongin-si, Republic of Korea

Correspondence to: Jörg Gumbel (gumbel@misu.su.se)

Abstract. Global three-dimensional data are a key to understanding gravity waves ~~interactions~~ in the mesosphere and lower thermosphere. MATS (Mesospheric Airglow/Aerosol Tomography and Spectroscopy) is a new Swedish satellite mission that addresses this need. It applies space-borne limb imaging in combination with tomographic and spectroscopic analysis to obtain gravity wave data on relevant spatial scales. Primary measurement targets are O_2 Atmospheric Band dayglow and nightglow in the near infrared, and sunlight scattered from noctilucent clouds in the ultraviolet. While tomography provides horizontally and vertically resolved data, spectroscopy allows analysis in terms of mesospheric temperature, composition, and cloud properties. Based on these dynamical tracers, MATS will produce a climatology on wave spectra during a 2-year mission. Major scientific objectives concern a characterization of gravity waves and their interaction~~s~~ with larger scale waves and mean flow in the mesosphere and lower thermosphere, as well as their relationship to dynamical conditions in the lower and upper atmosphere. MATS is currently being prepared for launch in late 2019. This paper provides an overview over scientific goals, measurement concepts, instruments, and analysis ideas.

1 Introduction

1.1 Gravity waves in the mesosphere and lower thermosphere

Atmospheric gravity waves are small scale buoyancy waves that can transport momentum and energy over large distances in the atmosphere. Primary sources are disturbances in the troposphere such as flow over topography, convective systems or jets. Conservation of energy makes the amplitude of the gravity waves grow as they propagate upward towards less dense altitudes. As the waves dissipate, they deposit their momentum and energy onto the background atmosphere. This in turn affects the atmosphere over a wide range of scales, from the local generation of turbulence to the forcing of a large scale circulation (Fritts and Alexander, 2003; Alexander et al., 2010). This dynamical forcing is most prominent in the mesosphere and lower thermosphere (MLT), at altitudes of typically 50-130 km. Here a large fraction of upward propagating gravity waves reach their maximum amplitudes and break. The resulting dynamical forcing causes a global-scale circulation in the mesosphere with strong upwelling ~~at~~ in the summer ~~pole~~ polar region and downwelling ~~at~~ in the winter ~~pole~~ polar region (Lindzen, 1981; Holton, 1982). Adiabatic cooling and heating connected to this circulation causes thermal conditions in the mesosphere to deviate far from radiative equilibrium. As one consequence, the polar summer mesosphere is turned into the coldest place on Earth, with temperatures reaching well below 130 K despite permanently sunlit conditions. This makes the region the home of the highest clouds on Earth, noctilucent clouds (NLC) (Thomas, 1991; Karlsson and Shepherd, 2018).

The role of gravity waves is further complicated as they interact with the background flow on their way through the middle atmosphere. This leads to an altitude-dependent filtering of the gravity wave spectrum by the wind field (e.g., Fritts and Alexander, 2003), including the wind patterns connected to planetary waves or tidal waves. The gravity wave spectrum arriving at higher altitudes thus carries an imprint of the dynamics at lower altitudes. This leads to a number of interesting teleconnections that can link conditions in widely separated regions of the atmosphere. Examples are the control of the summer mesosphere by lower atmospheric conditions in terms of inter- and intra-hemispheric coupling (Gumbel and Karlsson, 2011; Körnich and Becker, 2010). Interactions between gravity waves and the mean flow can also give rise to a generation of secondary waves in the mesosphere. Gravity waves can generate planetary waves, either directly through zonally non-uniform dissipation (Holton, 1984), or indirectly through induced baroclinic instability in the vicinity of jets (Plumb, 1983; Sato and Nomoto, 2015). The breakdown of gravity waves can also generate secondary gravity waves, propagating both upward and downward. This happens through localized momentum and energy fluxes, which in turn create strong body forces and imbalances (Vadas et al., 2003; Fritts et al., 2006; Becker and Vadas, 2018).

While today the basic nature of the wave-driven circulation of the middle atmosphere is ~~today~~ understood, important mechanisms and interactions remain to be quantified. Most notably, this concerns wave sources, wave dissipation, and the resulting forcing of the mean flow. ~~Decisive quantities for the forcing of the mean flow are~~ A decisive quantity to be specified is the directional momentum flux, ~~and the~~ including its altitude dependence ~~distribution of wave dissipation~~ and its spectral distribution with regard to horizontal and vertical wavelengths. Today, many general circulation models can explicitly simulate gravity waves with longer horizontal and vertical wavelengths, while shorter sub-grid waves need to be parameterized e.g. in terms of the "wave drag" that they exert on the mean flow (Alexander et al., 2010; Geller et al, 2013). Rather than accounting for the detailed underlying physics, these wave parameterizations are often used as a means of tuning the model to ensure realistic output e.g. in terms of middle atmospheric wind fields or temperature fields. Recently, important steps have been taken towards completely gravity-wave-resolving general circulation models (Watanabe et al., 2015; Becker and Vadas, 2018). Complementary to these developments, ray-tracing models are important tools for case studies of wave events and comparisons to specific observational datasets (e.g., Marks and Eckerman, 1995; Kalisch et al., 2014). A goal of ongoing model developments is to explicitly describe the entire chain from the lower atmospheric source region, via the lower and middle atmospheric wave filtering, to the wave effects in the MLT. Only wave-resolved simulations can be expected to describe the physics of e.g. intermittent wave interactions, energy cascading in the Lorenz energy cycle, or turbulence generation (Becker, 2012).

Observational data are critical for supporting such model developments, in particular in the MLT where gravity wave effects are most evident. Unfortunately, we are today lacking global observations of wave spectra arriving in the MLT, and even more so of the contribution of different parts of the wave spectra to momentum transfer. Such observations are desirable not only to constrain model results directly in the MLT. Rather, gravity wave observations in the MLT ~~data~~ can serve as a benchmark for testing wave implementations throughout the lower and middle atmosphere: general circulation models need to correctly describe the chain of wave processes at all altitudes in order to correctly reproduce resulting gravity wave properties observed in the MLT. In addition to providing a relevant database of gravity wave spectra, MLT studies are also needed that allow investigations of the three-dimensional structure of wave propagation. An important example is the refraction of gravity waves in the vicinity of the mesospheric jet (Sato et al., 2009, Preusse et al., 2009, Ern et al., 2011). Other three-dimensional propagation effects concern the interaction of gravity waves with the polar vortex (McLandress et al., 2012; de Wit et al., 2014; Wright et al., 2017) or the suggested refraction of gravity waves during sudden stratospheric warmings (Thurairajah et al., 2014, Ern et al., 2016).

A field of particular interest is the relationship between gravity waves and NLC. As described above, the gravity-wave-driven large-scale circulation is the very cause of extremely cold polar summer mesopause region, and thus a pre-condition for the formation of NLC. On more local scales, gravity-wave-induced variations of temperature and vertical wind strongly affect NLC conditions, and can both cause, enhance or prohibit the formation of the clouds (e.g. Rapp et al., 2002; Kaifler et al., 2018). At the same time, ground-based and space-based observations of NLC are a primary source of our knowledge about gravity wave activity in middle atmosphere (e.g., Witt, 1962; Chandran et al., 2009; Rong et al., 2018; Gumbel and Karlsson, 2011). ~~Also concerning mesospheric ice formation and NLC,~~ Gravity waves may also play an important role in explaining ~~explanations are lacking for a number of~~ other dynamical NLC features like so-called ice fronts or ice voids (Megner et al., 2018).

While the above descriptions have focused on gravity wave interactions with larger scale waves and the mean flow from the lower atmosphere to the MLT, the importance of gravity waves extends well beyond these altitudes. The MLT can be regarded as a transition region where many fundamental changes occur in atmospheric properties. Examples are the transition from well-mixed, turbulent conditions to molecular diffusion, a transition to non-local thermodynamic equilibrium with a substantially increased lifetime of excited species, a transition to an extreme-UV radiative environment, or the transition to increasing importance of ionospheric processes. Various "layered phenomena" in the MLT can be regarded as manifestations of these transitions. Prominent phenomena include dayglow and nightglow, layers of metal, dust or ice, as well as various plasma processes – all demonstrating strong links to both below and above. Despite this fact, the altitude around 100 km has long been regarded as a dividing line between different research communities, separating the middle and upper atmosphere. This view has changed in recent decades, and has today been replaced by a strong interest in "whole atmosphere" model approaches that emphasize the connecting rather than the dividing role of the MLT (e.g., Roble, 2000; Marsh et al., 2007; Akmaev, 2011). Wave processes play a central role in this respect, and in bridging the atmospheric communities.

In addition to comprehensive whole atmosphere modeling efforts, there has been growing observational evidence of thermospheric and ionospheric responses to wave processes in the lower and middle atmosphere. The dynamical morphology of thermosphere and ionosphere has been shown to be strongly connected to tidal waves (e.g., Anderson, 1981; Oberheide et al., 2009), but also to planetary waves (e.g., Chen, 1992; Forbes and Leveroni, 1992) and gravity waves (e.g., Röttger, 1977; Park et al., 2014; Forbes et al., 2016; Trinh et al., 2018). A basic open question concerns the relative importance of primary and secondary waves in propagating from the middle atmosphere to the thermosphere and ionosphere (Becker and Vadas, 2017). In the altitude range 100-300 km, gravity waves have been shown to create temperature variations of 50 K and density variations of 10-25% over spatial scales of tens to hundreds of kilometres (Vadas and Liu, 2013). As the gravity waves interact with the background flow before reaching these altitudes, fingerprints of middle atmospheric circulation systems have been revealed well into the thermosphere and ionosphere (Siskind et al., 2012). A prominent example is dynamic coupling suggested to occur during sudden stratospheric warmings (Funke et al., 2010; Chau et al., 2011). Akmaev (2011) estimates that more than half of the regular daily and seasonal variability in the thermosphere and ionosphere is forced from below. Akmaev further concludes that the availability of global data on MLT dynamics and variability is a limiting factor for future scientific progress, thus contrasting the MLT to the "data-rich" lower atmosphere and upper thermosphere.

In summary, there is substantial need for global observations of gravity waves in the mesosphere and lower thermosphere. These datasets are needed to support and verify ongoing developments of general circulation models, concerning both gravity wave parameterizations and gravity-wave-resolved implementations. These datasets should provide: (1) information about horizontal (and vertical) wave spectra in order to identify the dominant scales that govern interactions with the mean flow, larger scale waves, and possibly secondary waves, (2) information about directional momentum flux as decisive quantity for these interactions, and (3) three-dimensional wave information in order to address detailed propagation and refraction effects in the vicinity relevant dynamical structures.

1.2 Satellite measurements of gravity waves

What is the current status regarding ~~Where are we concerning~~ such global observations of gravity waves in the MLT? ~~Various~~ Several satellite missions have provided data on MLT structures that have been analysed in terms of wave activity on various scales. Most of these apply limb-viewing geometries in a number of spectral ranges. On the TIMED satellite, infrared limb measurements by the SABER instrument provide species and temperature distributions that allow for retrievals of gravity waves and planetary waves (Krebsbach and Preusse, 2007; Forbes et al., 2009; Preusse et al., 2009). The TIDI instrument provides MLT gravity wave data in terms of airglow Doppler wind measurements (Liu et al., 2009). On the ENVISAT satellite, infrared limb emission measurements by the MIPAS instrument cover the MLT and can provide large-scale wave structures that could also be traced into the thermosphere (Funke et al., 2010). From the SOFIE instrument onboard the AIM satellite, gravity wave potential energy is inferred based on infrared solar occultation temperature retrievals throughout the stratosphere and mesosphere (Liu et al., 2014). Measurements by the SCIAMACHY instrument have been analysed in terms of MLT planetary wave structures in noctilucent clouds (von Savigny et al., 2007). On the Aura satellite, microwave limb measurements by the MLS instrument have provided mesospheric planetary wave data based on composition, temperature and Doppler wind analysis (Limpasuvan et al., 2005; Wu et al., 2008). The above limb sounders can provide vertical retrieval resolutions down to a few kilometers. However, all gravity wave analysis from these limb measurements suffers from sparse horizontal sampling and the long line-of-sight integration, largely restricting the analysis to horizontal wavelengths exceeding several hundred kilometres.

Complementary to the above limb datasets, nadir-viewing satellite ~~instruments~~ measurements have been analysed in terms of waves in the MLT, primarily focusing on horizontal wave structures. These studies employ observations of either noctilucent clouds or airglow layers. Basic wave parameters have been inferred from NLC observations by the UVIST instrument onboard the MSX satellite (Carbary et al., 2000). On the AIM satellite, the CIPS instrument has provided comprehensive gravity wave information from near-nadir imaging of NLC, resulting in wave climatologies covering horizontal wavelengths both above 100 km (Rusch et al., 2008; Chandran et al., 2009) and below 100 km (Rong et al., 2018). MLT gravity wave analysis based on nadir nightglow observations has been reported from the VIIRS instrument onboard the NOAA/NASA Suomi satellite (Yue et al., 2014; Miller et al., 2015; Azeem et al., 2015), and the IMAP/VISI instrument on-board the International Space Station (Perwitasari et al., 2016). All gravity wave analysis from these nadir imagers is largely restricted to information about horizontal wavelengths in the observed layer. For NLC, however, information about vertical structures has recently been obtained by applying tomographic methods to the different viewing angles available from the AIM/CIPS observations (Hart et al., 2018).

For a more complete gravity wave analysis, three-dimensional retrievals are desirable that provide spatial structures ~~both horizontal wavelengths~~ extending both ~~below~~ shorter than 100 km in horizontal wavelength and shorter than ~~vertical wavelengths extending below~~ 10 km in vertical wavelength (Preusse et al., 2008). Being limited by either the limb or nadir geometry, we are so far lacking such three-dimensional gravity wave data in the MLT. In the stratosphere, techniques have been developed to overcome these limitations. The AIRS instrument on-board the AQUA satellite measures upwelling radiation in a large number of spectral channels, and gravity waves have been retrieved from the upper troposphere to the mid-stratosphere (Hoffmann and Alexander, 2009; Gong et al., 2012). Additional techniques have been developed to maximize horizontal wave information from AIRS, utilizing either across-track nadir scans (Wright et al., 2017) or data from multiple satellite tracks (Ern et al., 2017). Enhanced horizontal information can also be obtained by combining data from several sounding instruments, like multiple GPS radio occultations (Wang and Alexander, 2010; Schmidt et al., 2016), or combined data from the HIRDLS instrument on-board the Aura satellite and radio occultations (Alexander, 2015).

The ultimate way to obtain three-dimensional information about gravity waves is to apply tomographic techniques. Tomographic retrievals have been applied to the limb-scanning instruments MIPAS on-board ENVISAT (Carlotti et al., 2001; Steck et al., 2005) and MLS on-board Aura (Livesey et al., 2006). In the mesosphere, tomographic retrieval has been applied to the limb-scanning Odin satellite to study NLCs by the OSIRIS optical spectrograph (Hultgren et al., 2013; Hultgren and

Gumbel, 2014), and water vapour and temperature by the SMR microwave instrument (Christensen et al., 2015; 2016). For instruments specifically designed for tomography, limb imaging is preferable over the above limb scanning techniques. In this way, the number of lines of sight through a given atmospheric volume can be maximized. This has been utilized by the infrared limb imager of the OSIRIS instrument on-board Odin (Degenstein et al., 2003, 2004), and by the airborne GLORIA instrument (Ungermann et al., 2011; Kaufmann et al., 2015). Limb imaging also ~~opens for a transition~~ provides the possibility to go from two-dimensional to fully three-dimensional tomography. Ungermann et al. (2010) investigated requirements for gravity wave retrievals in the troposphere and stratosphere, emphasising the need for a fully three-dimensional tomographic analysis. Krisch et al. (2017) discussed tomographic retrieval with special emphasis on the limited range of observation angles that are typically available from limb measurements.

In this paper, we describe a new satellite mission aiming at three-dimensional tomographic studies of gravity waves and other structures in the upper mesosphere and lower thermosphere. The MATS satellite will perform limb-imaging of the O_2 Atmospheric Band airglow in the near-infrared and of NLC in the ultraviolet. In combination with the tomography, spectroscopic techniques will be applied to infer atmospheric temperature and composition from the O_2 emissions, and microphysical cloud properties from the NLC measurements. A complementary camera will provide nadir imaging of structures in the O_2 Atmospheric Band nightglow on smaller spatial scales. A similar mission with focus on the O_2 Atmospheric Band nightglow has recently been described by Song et al. (2017). As compared to the pure limb imaging by MATS, Song et al. envisage tomographic retrievals utilizing both limb and sub-limb viewing.

The next section describes the basic ideas of the MATS mission, with focus on scientific objectives and resulting instrument requirements. Section 3 provides details about the instrument design. Section 4 introduces the retrieval ideas behind MATS and the basic data processing. Section 5 describes operational planning. Section 6 concludes with a summary and some perspectives towards scientific collaboration. Note that the idea of this paper is to provide a general overview over the mission. More comprehensive details about instruments, retrieval methods and scientific analysis will be published in separate papers.

2 The MATS satellite mission

2.1 Scientific Objectives

The primary goal of MATS is to determine the global distribution of gravity waves and other structures in the MLT over a wide range of spatial scales. Primary measurement targets are airglow in the O_2 Atmospheric band and sunlight scattered from NLC. These emissions will be measured in an altitude range 75-110 km, and are to be analysed in terms of wave structures with horizontal wavelengths from tens of kilometres to global scales, and vertical wavelengths from 1 to 20 km. Over a period of two years, MATS will thus build up a geographical and seasonal climatology of wave activity in the MLT. This database will then be the starting point for scientific analysis in various directions. Relating back to the overview in Section 1, major scientific questions are:

- What gravity wave spectra are present in the MLT, and how are these related to tropospheric sources and circulation conditions in the lower and middle atmosphere? These questions are tightly connected to wave-wave interactions such as filtering by planetary wave activity and in-situ generation of secondary waves.
- To what extent does MLT wave activity affect processes in the thermosphere and ionosphere? As part of this objective, methods need to be developed that utilize the mapping of mesospheric wave activity as an input to studies of thermospheric variability.
- How can explicit and parameterized implementations of gravity waves be improved in ~~in~~ atmospheric models? This relates back to the quest to reduce large uncertainties in current descriptions of wave sources, wave propagation, and wave interactions.

While the MATS gravity wave climatology will be the starting point for addressing these questions, complementary input from other sources will be important. This includes in particular meteorological reanalysis data, ionospheric monitoring systems, and other dedicated missions that provide data beyond the altitude range of the MATS measurements.

As described above, NLC are one of the measurement targets of MATS. Since the pioneering days of NLC research, these clouds have transformed from a basic research object to a valuable research tool when it comes to remote sensing of the state of the MLT. Nonetheless, beyond using NLC as a convenient tracer for gravity wave studies, the MATS science objectives ~~will~~ also include ~~address basic science questions concerning~~ NLC in their own right:

- How are NLC affected by gravity waves and other transient processes in the MLT? This concerns both the microphysics of ice particles and the resulting evolution of observable cloud structures.

2.2 Measurement concepts

The above scientific objectives define the requirements on the measurements that MATS will perform. Tomography is the basis for obtaining three-dimensional information on spatial scales that are relevant for gravity wave studies. The tomographic retrieval needs input in terms of multiple line-of-sight observations through a given atmospheric volume. This is achieved by a limb imager that observes the atmosphere along the Earth's tangent direction, with a field of view covering tangent altitudes between 75 and 110 km, and 300 km across track. Figure 1 illustrates the observation geometry. In order to tomographically retrieve gravity wave information in the MLT, we need to utilize atmospheric emissions that are both sufficiently bright and susceptible to gravity wave activity. In the case of MATS, we utilize airglow in the O_2 Atmospheric Band and scattering of sunlight by NLC. Both O_2 Atmospheric Band airglow and NLC feature horizontal and vertical structures that are a direct response to gravity wave activity. As an additional benefit, both phenomena allow for a deeper analysis by applying spectroscopic techniques.

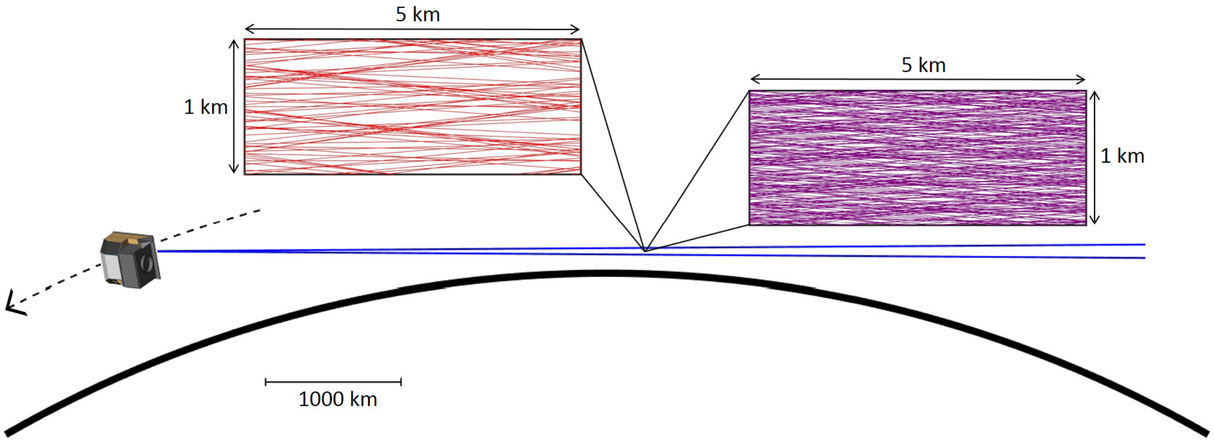

Figure 1. Illustration of the MATS limb observation geometry. From an orbit altitude of 585 km, the vertical field of view of the limb instrument covers nominal tangent altitudes from 75 to 110 km. The smaller inlays show examples of lines-of-sight filling a section of 5×1 km in the orbit plane. ~~The density of the lines-of-sight is representative for the binned image pixels in an O_2 Atmospheric Band channel (left) and an NLC channel (right).~~The red lines in the left inlay are representative for the density of lines-of-sight through a given measurement volume, taking into account the larger binned image pixel size and the longer readout interval in an O_2 Atmospheric Band channel. The violet lines in the right inlay are representative for the density of lines-of-sight through a given measurement volume, taking into account the smaller binned image pixel size and the shorter readout interval in an NLC channel.

On MATS, the O_2 Atmospheric Band is measured using four spectral channels in the near infrared between 750 and 775 nm (see Table 4 for details). Measurements will be performed both during daytime (dayglow) and nighttime (nightglow). As a primary step, the tomographic analysis will convert measured limb radiances to volume emission rates. Combining the four channels, subsequent spectroscopic analysis will utilize the rotational structure of the O_2 Atmospheric Band emission to infer temperature (Babcock and Herzberg, 1948; Sheese et al., 2010). At the same time, the total volume emission rate in the O_2 Atmospheric Band can be analysed in terms of odd oxygen densities: The Atmospheric Band nightglow provides a direct measure of atomic oxygen density (McDade et al., 1986; Murtagh et al., 1990). The Atmospheric Band dayglow, on the other hand, provides information about ozone density (Evans et al., 1988; Mlynczak et al., 2001), which in turn is related to atomic oxygen through photochemical equilibrium. Gravity waves in the MLT can be inferred from these measurements by observing patterns in either airglow volume emission, odd oxygen, or temperature. Among these, analysing gravity waves in the temperature field is most beneficial as temperature is directly connected to the basic state of the atmosphere and as gravity wave momentum flux becomes accessible (Ern et al, 2004~~; Fritts et al., 2014~~). To this end, temperature amplitudes as well as horizontal and vertical wavelengths need to be inferred from the measurements.

NLC are measured by MATS using two spectral channels in the ultraviolet at 270 and 305 nm. While imaging at one wavelength is sufficient for analysing global NLC variations and local NLC structures, the use of two wavelengths gives the additional benefit of accessing particle sizes and ice content. To this end, the observed spectral dependence of NLC signal is fitted in terms of an Ångström exponent and compared to numerical scattering simulations (von Savigny et al., 2005; Karlsson and Gumbel, 2005). For typical NLC particle sizes, observations in the ultraviolet are preferable as they push the scattering deeper into the Mie regime, thus maximizing the amount of information that can be inferred from spectral measurements. In addition, wavelengths below 310 nm are efficiently absorbed by the stratospheric ozone layer, and are therefore chosen to avoid complications due to upwelling radiation. For MATS, the concrete wavelengths 270 nm and 305 nm are chosen both to ensure a sensitive retrieval in the NLC particle size range of interest (Section 4.6), and to minimize potential perturbations due to atmospheric emission features (airglow, aurora). The tomographic NLC data will be the basis for gravity wave analysis in terms of horizontal wavelengths. The vertical structure of the NLC is strongly determined by the microphysics that governs cloud growth and sedimentation (Rapp and Thomas, 2006). The tomography will provide detailed insights in this vertical NLC evolution, including its possible modification by wave activity (Hultgren and Gumbel, 2014; Megner et al., 2016; Gao et al., 2018). However, since the vertical structure of the narrow NLC layers is dominated by microphysics rather than dynamical processes, a retrieval of vertical wavelengths of gravity waves will not be feasible from the NLC data.

The limb instrument will be described in Section 3, and details of the tomographic and spectral retrievals will be given in Section 4. Table 1 summarizes the above retrieval products from the MATS limb measurements. The table also states the required precision and spatial resolution of these retrieval products. These requirement are defined by the need to infer relevant gravity wave data from these retrieval products, in accordance with the overall objectives listed in the Section 2.1. Note that typical values are given for precision and resolution. These parameteres depend on the altitude-dependent signal strengths. They are also adjustable as e.g. enhanced image binning can improve precision at the cost of resolution. These trade-offs will be further illustrated in the following sections.

	O_2 Atmospheric Band dayglow/nightglow			**NLC**	
	Emission rates	**Temperature**	**O ~~/~~and O_3 abundance**	**Brightness** (scattering coefficient)	**Particle sizes** (Ångström exponent)
Temporal coverage	all seasons	all seasons	all seasons	summer	summer
Geographical coverage	global	global	global	poleward of 45°	poleward of 45°
Altitudes	75-110 km	75-110 km	75-110 km	80-86 km	80-86 km
Precision	1-5 %	2-5 K (day) 5-20 K (night)	1-5 %	2-5 %	0.25
Retrieval resolution (along track × across track × vertical)	60×20×1 km	60×20×1 km	60×20×1 km	60×10×0.5 km	60×10×0.5 km

Table 1: Products of the tomographic/spectroscopic retrievals from the MATS limb measurements. These serve as input to subsequent wave analysis.

In addition to these MATS limb measurements, an auxiliary nadir imager will take pictures of the O_2 Atmospheric Band emission from below the satellite. This provides complementary information on smaller spatial scales down to 10-20 km horizontal resolution, albeit restricted to a detection of structures rather than a detailed spectroscopic analysis. During sunlit (or moonlit) conditions, nadir measurements of airglow layers get drowned in background light from the lower atmosphere. Gravity wave data from the MATS nadir camera will therefore ~~largely~~ be restricted to moonless nights~~time conditions~~. The near-terminator orbit of MATS is not optimal for such nightglow studies as sufficiently dark measurement conditions will only be available during the winter season at mid and high latitudes. From the ground, nightglow imaging is a standard technique for local measurements of gravity waves in the MLT (~~{~~e.g., Taylor et al., 1997; Espy et al., 2004)~~}~~. An obvious advantage of satellite measurements is global coverage, however, this comes with the disadvantage of lacking temporal coverage at a given location. Also, nadir imaging from a moving satellite is subject to image smearing (motion blur), thus implying a restriction to short integration times and strong wave features~~ and short integration times~~.

2.3 Mission development

Original ideas for MATS date back longer than the current project development. A first mission concept was developed by Jacek Stegman and Donal Murtagh at Stockholm University in the 1990s, then under the name "Mesospheric Airglow Transient Signatures (MATS)". An important heritage for MATS is also the Odin satellite mission, both concerning satellite, instrument, and operational concepts (Murtagh et al., 2002; Lle~~l~~wellyn et al., 2004). For the Optical Spectrograph and InfraRed Imager System (OSIRIS) on-board Odin, tomographic ideas were developed by Degenstein et al. (2003; 2004). In 2010, special "tomographic" scan modes were developed for Odin, covering a limited tangent altitude range of about 75-90 km with relatively high horizontal repetition rate. These measurement provided input to tomographic and spectroscopic retrievals (Hultgren and Gumbel, 2014) that served as important tests for the MATS mission development.

The current MATS satellite mission was developed in response to a call by the Swedish National Space Agency concerning "Innovative low-cost research satellite missions". MATS was selected after going through an initial Mission Definition Phase in 2014.

An important basis for MATS is the InnoSat satellite platform developed by OHB Sweden and ÅAC Microtec (Larsson et al., 2016). InnoSat has been designed as a "universal" microsatellite platform that can host a variety of different payloads for aeronomy or astronomy research in low-earth orbit. MATS is the first scientific mission to use InnoSat. As a consequence, much of the development of platform and payload have been carried out in parallel. MATS has been designed to use the "baseline configuration" of InnoSat. Table 2 lists important parameters that define this configuration. All parameters in Table 2 constitute boundary conditions for the design and performance of MATS, as will be illuminated further in Sections 3 and 4.

Mass	50 kg (incl. 20 kg payload)
Size	85×70×55 cm
Power	45 W on orbit average
Data volume	180 MBytes per day
Pointing accuracy (in terms of limb altitude)	5 km pointing error (target) 0.5 km knowledge error (reconstruction)
Orbit	sun-synchronous, near-terminator, polar orbit
Nominal lifetime	2 years

Table 2: Selected parameters of the InnoSat satellite platform in its baseline configuration.

Behind the development of the MATS instruments and scientific mission is an Instrument Consortium comprising Stockholm University, Calmers University of Technology in Göteborg and the Royal Institute of Technology in Stockholm, in collaboration with Omnisys Instruments (Göteborg), Molflow (Göteborg), and Kyung Hee University (Republic of Korea). This is complemented by a Platform Consortium comprising OHB Sweden in Stockholm and ÅAC Microtec in Uppsala, the companies behind InnoSat. The MATS satellite is currently in preparation for a launch in late 2019. The launch will take place in a piggyback configuration on a Soyuz-2-1b rocket from Vostochny in Eastern Russia. The nominal altitude of the orbit is 585 km. The nominal local time of the equator passage is 6:30 and 18:30, thus providing a "near-terminator" orbit.

3 Instrument Design

3.1 Overview

The MATS payload comprises four optical instruments: The 6-channel limb imager and the nadir camera measure mesospheric emissions, as introduced in the previous section. A pair of nadir-viewing photometers measures upwelling radiation from the Earth surface and lower atmosphere, in support of the limb instrument analysis. A star-tracking camera directed in the opposite direction of the limb imager ensures accurate pointing of the satellite. Figure 2 shows the overall configuration.

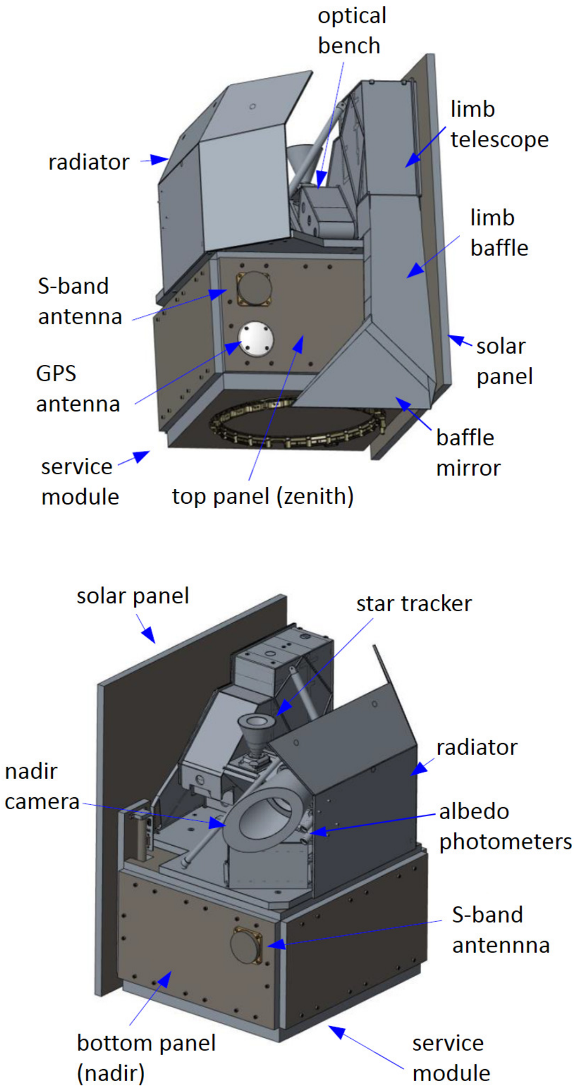

Figure 2. Layout of the MATS satellite.

The sun-synchronous polar orbit with nominal equator passage near 06:30 and 18:30 local time is beneficial for an efficient satellite design. It ensures that satellite receives sunlight largely during the entire mission, and that a solar panel mounted at one side of the platform is sufficient to make use of this sunlight. In addition, instruments and electronics will be shaded behind the solar panels during the mission. As for the field of view, the satellite will nominally be oriented so that the limb instrument looks backwards along the orbit. This provides the necessary overlap between subsequent images as input to the tomography retrieval.

3.2 Limb instrument

Since the goal is to investigate both NLCs and O_2 Atmospheric Band emission, two separate wavelength regions will be measured by MATS. As described in Section 2.2, two UV channels will be used for the NLC study. To measure the Atmospheric Band emission, two main channels are used: a wideband channel covering the entire 0-0 vibrational band, and a narrowband channel covering only the centre. In order to quantify the effect of background radiation and straylight on the Atmospheric Band measurements, a set of ancillary measurements are done using two background IR channels of the limb imager, as well as the pair of nadir-looking photometers that provide information about upwelling radiation both within and outside the Atmospheric Band. In order to achieve the MATS measurement objectives (Table 1), four basic tasks have been central to the limb instrument design: imaging quality, sensitivity (signal-to-noise ratio), spectral separation, and straylight suppression. Boundary conditions for the design are defined by the InnoSat satellite platform in terms of mass, dimensions, power etc. (Table 2). Figure 3 shows the overall layout of the limb imager.

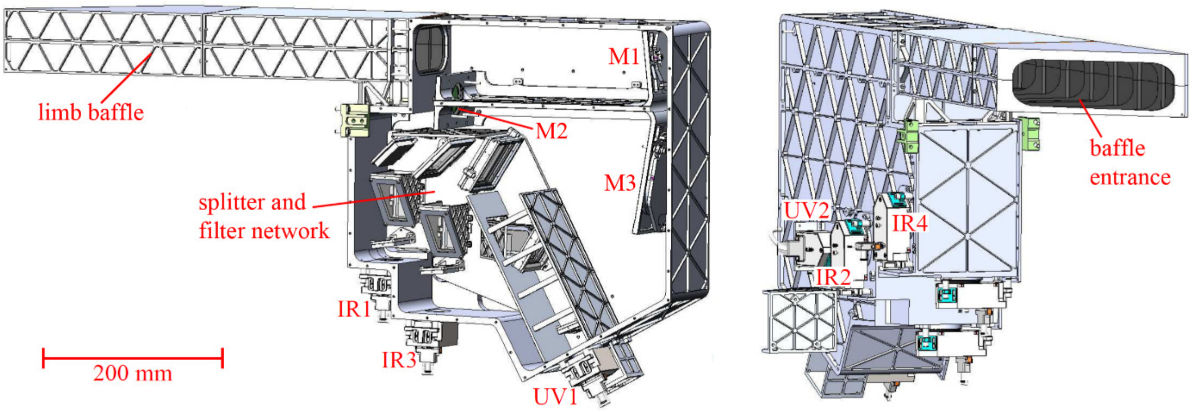

Figure 3. Overview of the MATS limb imager with one of the side covers removed (Hammaer et al., 2018). Marked in the image are the telescope mirrors M1-M3, as well as the CCDs IR1-IR4 and UV1-UV2 for the six spectral channels.

3.2.1 Telescope

The limb instrument is based on a single off-axis three-mirror reflective telescope (f/D = 7.3) with a field of view (FOV) of 5.67° × 0.91° (Hammar et al., 2019). The mirrors are manufactured by Millpond ApS with fully free form surfaces. They are made of aluminium with the active surfaces defined using diamond turning. The free form design was optimized to achieve diffraction-limited imaging. Inter-mirror distances and angles were chosen to satisfy the linear-astigmatism-free condition. Linear astigmatism is the dominant aberration of off-axis reflecting telescopes and must be eliminated to obtain a wide field of view (Chang, 2015). A summary of properties of the limb telescope is found in Table 3.

Type	Linear-astigmatism-free off-axis three-mirror reflective
Mirrors	diamond turned aluminium with protective UV coating, 3 nm rms
Field of view	5.67° × 0.91° (250 km × 40 km)
Entrance pupil	9.6 cm^2
Focal length	260 mm
f / D	7.3
Aperture stop	located on the secondary mirror

Table 3. Overview of optical properties of the MATS limb telescope.

3.2.2 Splitter and filter network

Following the telescope is a network of dichroic beam splitters and thin-film interference filters that are used to achieve the desired spectral selection. As the first element, a beamsplitter BS-UV-IR reflects wavelengths below 345 nm towards the UV part of the instruments, while longer wavelengths are transmitted towards the infrared part. Figure 4 shows the detailed distribution of spectral channels and optical elements. Each of the instrument's six channels uses a broadband filter to remove out-of-band signals, followed by a narrowband filter that ultimately defines the wavelengths transmitted to the image sensors. In addition, two folding mirrors are used to keep the optical components within the InnoSat platform envelop. Optical tests performed at breadboard and prototype level shows that the resolution requirement for the IR channels are fulfilled, while more careful mirror alignment is needed for the flight model to meet the imaging requirements of the UV channels.

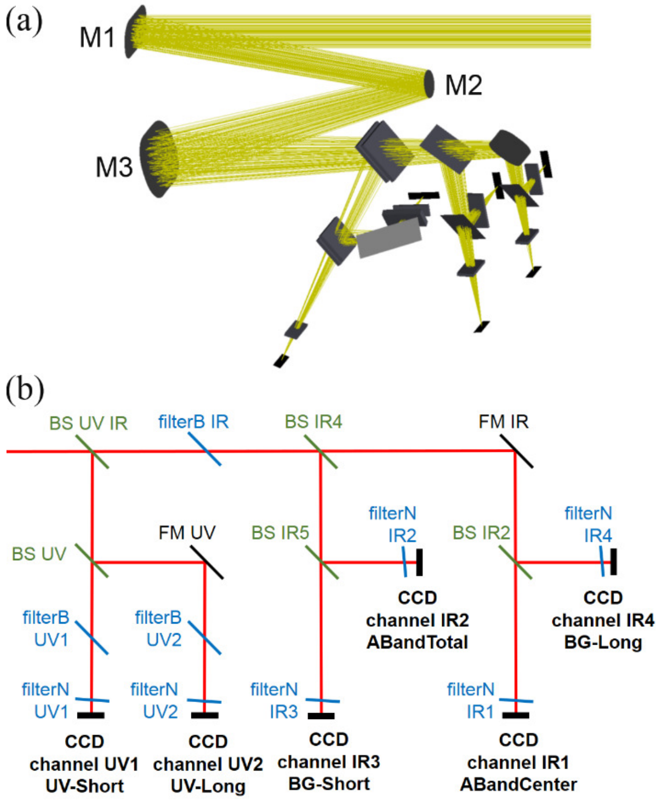

Figure 4. Overview of the optical paths in the limb imager. (a) Geometrical distribution of the optical elements, including the three telescope mirrors M1-M3. (b) Schematic of the channel layout with beamsplitters (BS), broad filters (filterB), narrow filters (filterN), folding mirrors (FM), and CCDs. See also Figure 3.

Designation	Central wavelength	Band-width	Tangent altitudes	Resolution (Imaging)	Resolution (Binning)	Signal/Noise Ratio
UV1-short	270 nm	3 nm	70-90 km	0.2 km	0.2×5 km	100
UV2-long	304.5 nm	3 nm	70-90 km	0.2 km	0.2×5 km	100
IR1-ABand-centre	762 nm	3.5 nm	75-110 km	0.4 km	0.4×10 km	500
IR2-ABand-total	763 nm	8 nm	75-110 km	0.4 km	0.4×10 km	500
IR3-BG-short	754 nm	3 nm	75-110 km	0.8 km	0.8×50 km	500
IR4-BG-long	772 nm	3 nm	75-110 km	0.8 km	0.8×50 km	500
Nadir	762 nm	8 nm	nadir	10 km	10×15 km	100

Table 4. Overview of optical properties of the MATS limb and nadir channels. The image resolution of the channels is specified in two ways: Imaging refers to the imaging quality of the optics in terms of the full width at half maximum of the point spread function. Binning refers to the size of the recorded image pixels after nominal binning on the CCD. Pixel sizes are given as vertical×horizontal for the limb channel, and as across track × along track (including motion blur) for the nadir channel.

3.2.3 Baffle design

One of the major design drivers for the limb instrument has been to minimize the impact of straylight from outside the field of view. This task is critical considering that the bright lower atmosphere is only 1-2° below the nominal mesospheric field of view. Central to the straylight handling is a long (>650 mm) baffle in front of the primary telescope mirror. To minimise the reflections inside the baffle, it is coated internally with Vantablack S-VIS, which has a reflectivity of less than 0.6% in the wavelength regions relevant for MATS. Furthermore, the limb housing and all mounting structures are coated using a black nickel (Hammar et al., 2018). During most of the mission, the baffle entrance will be in the shadow of the solar panel. However, during some high-latitude summer conditions, the sun can illuminate satellite structures near the baffle. In order to minimize the risk of straylight entering the baffle, a plane mirror is placed in front of the baffle entrance (Figure 2). As opposed to (black) surfaces that can scatter incident light in uncontrolled ways, this "baffle mirror" has been designed to reflect sunlight away from the instrument.

Since the MATS limb telescope lacks a field stop, Lyot stops are used in front of each image sensor. In addition, all sensors are deeply embedded in the structure. These measures ensure that the critical paths from the primary and secondary mirrors are removed. Furthermore, the inter-mirror distances were chosen to be as large as possible while still fitting into the available payload volume. By doing so, the subtended angles between the mirrors were minimized, which, in turn, minimizes the throughput of scattered light emanating from outside the nominal field of view.

To verify the performance of the stray-light suppression, a combination of experimental testing and modelling of the instrument in Zemax Opticstudio have been carried out (Hammar et al., 2018). From this, attenuations better than 10^{-5} are generally obtained for angles exceeding 1.5°, thus fulfilling the requirements for the mission.

3.2.4 Readout electronics

To record the incoming light, all channels use passively cooled back-lit CCD sensors (Teledyne E2V-CCD42-10). The data from each CCD are read out by a CCD Readout Box (CRB) with an instrument onboard computer (OBC) to handle the data. Two power and regulation units, located in the instrument electronics box together with the OBC, provide adjustable voltages for CCD operation, and multiplex the control of the CRB settings and the data readout, for up to four imaging channels. The OBC then compresses the image (if applicable) before handing over to the Innosat platform which manages the satellite downlink. The nominal image format will be compressed 12-bit JPEG images, while full resolution uncompressed image readout is also available for in-flight calibration purposes.

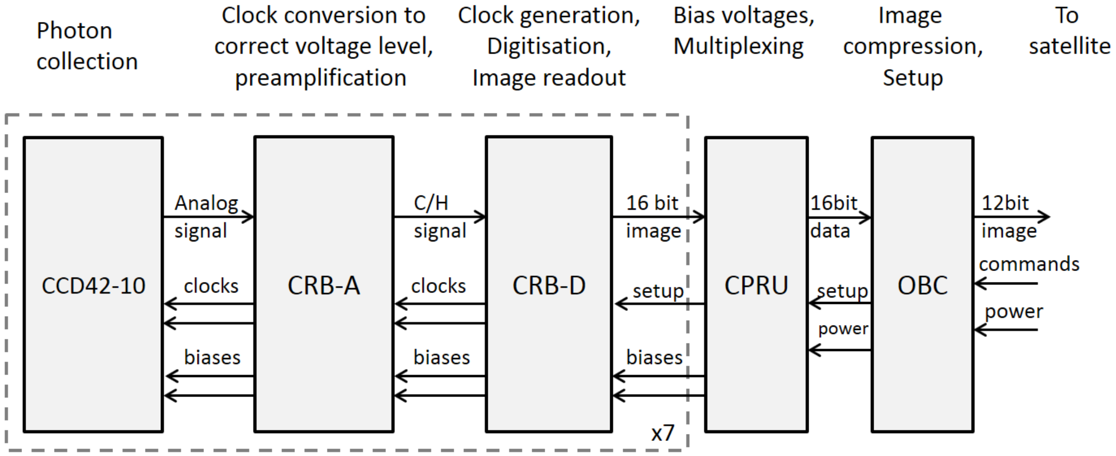

Figure 5. Overview of the MATS image acquisition. CCDs are controlled and read out by CCD Readout Boxes (CRB-A and CRB-D), connected to the CCD power regulation unit (CPRU) and onboard computer (OBC).

The CCD provides 512x2048 image pixels. The field of view of each limb channel occupies a wide (along the limb) and short (in the vertical direction) area of interest. CCD readout implies vertical shift of the image rows. To minimize the number of moving parts in the satellite no shutter is used in the instrument. As a consequence, the image rows continue being exposed during the readout shifting, resulting in image smearing. The effect of this is minimized by fast readout (using binning and skipping rows outside the region of interest) as well as correcting for smearing in post-processing (Section 4.2).

To minimize noise and interference in CCD readout, the read-out electronics is composed of two parts, analog and digital. The analog box (CRB-A) is located in immediate vicinity of the CCD. The function of CRB-A is to generate the necessary clock signals for the CCD and to provide signal conditioning for the CCD output signal. The clock signals are generated in the digital box (CRB-D, located together with the rest of the instrument electronics) with standard logic voltage level, and are converted to the voltages needed by the CCD inputs by dedicated gate drivers. The signal from the CCD is pre-amplified and handled by a clamp and hold circuit. The amplified analog signal is passed over a differential connection to the CRB-D, where it is digitized by a 16-bit ~~Analogue-to-Digital Converter~~ analog-to-digital converter (ADC) and stored in memory, available for transfer to the OBC. CRB-D uses a Field-Programmable Gate Array for generating the multiple clocks for the CCD, and sending the image to the OBC.

Since the different MATS channels and science modes have different requirements on the final image, the CRB firmware is flexible, allowing changing multiple settings of the readout, such as integration time, region of interest on the CCD, horizontal and vertical binning, or CCD output amplifier selection. An overview of the planned settings for the nominal science modes will be provided in Section ~~0~~ 5.

Exposure of the CCD to radiation in orbit will affect the dark current performance, which can be counteracted by adjusting the bias and clock voltages for the CCD in the power regulation unit. Hot pixels may develop on the CCD due to radiation. These can be excluded from binning, by flagging the columns that contain them as bad.

Giono et al. (2017) carried out performance measurements on a prototype version of the readout electronics, showing readout noise of about 50 e^- per CCD pixel using the high signal mode amplifier on the CCD. This can be further reduced to under 20 e^- per pixel by adjusting the pre-amplification gain and by using the low signal mode amplifier.

3.3 Albedo photometers

Each of the two albedo photometers consists of a two-lens telescope based on standard N-BK7 lenses, providing a field of view of 6°. In front of the telescope a pair of interference filters is placed on each photometer to discriminate against unwanted wavelengths. Baffles minimize straylight from outside the field of view. The detector is a Hamamatsu S1223-01 Si PIN photodiode. The system measures upcoming radiation at 759-767 nm and 752.5-755.5 nm, corresponding to the limb imager channels IR2-ABand-total and IR3-BG-short, respectively (Table 4). The signal to noise ratio is better than 100.

3.4 Nadir camera

The nadir camera is a Cooke triplet with an entrance pupil of 15 mm, and an effective focal length of 50.6 mm. Its field of view is 24.4° × 6.1°. From orbit, this covers an area of at least 200 km across track and 50 km along track at 100 km altitude. The design can resolve 10 × 10 km features at this altitude. Additional degradation occurs in the along-track direction due to smearing caused by the satellite movement during the exposure and read-out phase. Figure 6 shows a sample image taken by a prototype nadir camera from the ground. In orbit, the nadir measurements aim at nighttime conditions with the Sun located at least 10° below the horizon for a ground-based observer. However, under these conditions the satellite will be fully illuminated by the Sun, and straylight handling is thus essential for the nadir camera. Similar to the limb instrument, in addition to being mounted in the shadow of the solar panel, efficient straylight suppression for the nadir camera is achieved by a baffle with black coating on the inside.

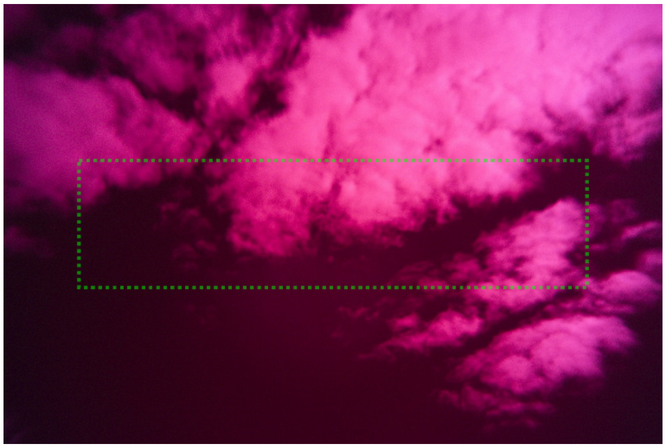

Figure 6. "First light" from a MATS instrument: ~~Ground~~ground-based photograph of a cloudy sky taken with the nadir objective mounted on a Canon camera house with a full frame sensor (35 mm). The dashed green rectangle denotes the cropped field of view as it will be seen with the MATS CCD sensor.

The readout of the nadir camera uses the same readout electronics as the limb instrument (Section 3.2.4), albeit operated in a different readout scheme. The satellite moves at a speed of about 7 km s^{-1}, and ~~In~~ in order to limit motion blur, nightglow images are taken with an exposure time no longer than 1 s. Exposures are taken and the CCD is read out at a rate sufficient to obtain overlapping images along the ground-track of the satellite. The result is a continuous nightglow image swath of width 200 km along the night-part of the orbit.

4 Data processing

4.1 Overview

The data produced by the instruments on board MATS requires several processing steps. The three major steps are:

Level 0: Geolocating the images and adding meta-data relevant for further processing.

Level 1: Calibrating the images (and photometer measurements) such that the pixel values reflect the actual measured radiance.

Level 2: Linking those values to the physical properties of the atmosphere via the 3D tomographic reconstruction and spectroscopy.

Since the first step is mainly an administrative step for further processing, only the Level 1 and 2 processing will be discussed in this paper. Focus will be on the limb instrument as the main instrument on MATS. Figure 7 shows the overall processing chain for the limb data.

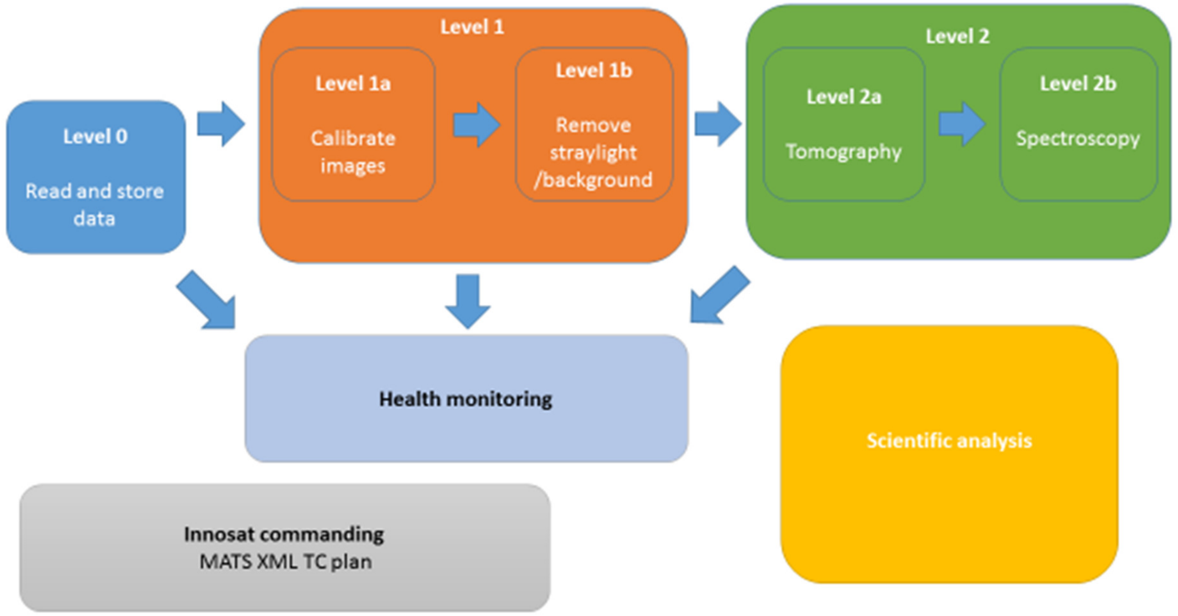

Figure 7. Overview of the data processing steps for the MATS limb imager.

4.2 Calibration of images

After geolocation and time-tagging, each image from the limb channels must be calibrated such that the image displays the radiance falling on each binned image pixel on the CCD~~ pixel~~. ~~The main effects that need to be accounted for during the calibration of the CCD images are: 1) biases in the readout electronics, 2) readout smearing, 3) dark current, and 4) flat field correction.~~ To do this, a parametrised model of the instrument has been developed that takes into account transmissivity of the optics, dark current and quantum efficiency variations with temperature, readout smearing, as well as readout bias and gain variations in the readout electronics. Each of these effects behaves differently, and must be measured and modelled separately. The parameters used in this modelling are a combination of pre-flight calibration measurements, and in-flight corrections to these parameters via special calibration modes (~~see~~ Section 5.2).

4.2.1 Readout bias

The bias produced by the readout electronics is determined for each image. This is done by means of blank pixel values, i.e. the signal from unexposed pixels in the readout register of the CCD. These pixels are shifted each time a row is read out, thus accumulating very little charge between consecutive rows. Two values, representing the average of the leading and trailing blank pixels, respectively, are recorded with each image as auxiliary information. Any inter-pixel variation in this offset will be compensated using a pixel-by-pixel map based on pre-flight calibration.

4.2.2 Readout smearing

In order to avoid risks associated with moving parts on the satellite, the CCDs have not been equipped with shutters. As a consequence, the CCD pixels are continuously illuminated, even during the image shifting associated with the readout, and are thus contaminated with signal from the "wrong" part of the image. To compensate for this effect, the image must be de-smeared by recursively correcting the pixel values in the CCD rows. While this process is completely deterministic for ideal noise-free measurements, it introduces minor image errors in the real data.

4.2.3 Dark current

The thermal energy of the CCD gives rise to electrons that are not due to incoming photons, but are nonetheless captured by the CCD's potential wells and counted as signal. The strong temperature dependence of this dark current is characterized pre-flight for the individual CCDs (Giorgi et al., 2017). In-flight measurements will monitor the detailed dark current properties of individual pixels throughout the mission.

4.2.4 ~~Flat field~~ Radiometric correction

~~Finally, the image is corrected for variations of the sensitivity across the image. Based on pre-flight calibration, this flat field correction accounts for variations of both the optical throughput through the limb instrument and the CCD quantum efficiency. The results is a map of the true pixel illumination.~~ The final step of the calibration involves estimating the amount of photons entering the telescope from the signal levels of the detected image. To do this, variations over the image of the optical throughout, inter-pixel variability in quantum efficiency, as well as variation in the gain of the readout electronics need to be accounted for. During preflight "flat field" calibrations, the telescope's optical throughput and the CCD's quantum efficiency will be determined together using measurements against a known radiance source. The readout gain (counts per electron) will be determined pre-flight at different temperatures. In orbit, the resulting radiative characteristics of the individual limb channels will be monitored using measurements of the moon, of stars (providing absolute calibration) and of molecular Rayleigh scattering from the Earth limb (providing relative inter-pixel variation).

4.3 Straylight and background removal

Before the limb radiances can be analysed in terms of airglow or NLCs, two unwanted contributions to the signal must be removed: background originating from within the nominal field of view, and straylight originating from outside the nominal field of view. Background from inside the field of view comprises both unwanted emissions (airglow, aurora) and scattered light (in particular molecular Rayleigh scattering). Straylight from outside the field of view can reach the CCDs by scattering in the baffle, scattering from imperfect or dusty surfaces of the optical elements (in particular the primary telescope mirror), and/or scattering from structures inside the instrument housing. Although the design of the limb instrument is optimized for out of field rejection, some straylight signal is to be expected. To remove this signal, both amplitude and non-uniformity across each CCD need to be estimated. As described in the following subsections, the amplitude will be estimated by combining information from several channels and tangent altitudes. The non-uniformity will be parameterized based on the straylight modelling and testing carried out prior to launch (Hammar et al., 2018).

The discrimination of unwanted and wanted radiances also needs to take account possible polarization effects. Based on pre-flight analysis, a potential source of polarisation sensitivity of the MATS instrument are the beamsplitters mounted at 45 degree to the incoming beam. Polarisation properties of the individual instrument channels are measured pre-flight, and can partly also be inferred in orbit, based on measurements against polarized atmospheric Rayleigh scattering under varying role angles of the satellite. Once the instrument's polarization properties are determined, their effect on the limb measurements can be taken into account in the retrieval. However, as different contributions to the total signal (airglow, NLC scattering, molecular scattering, straylight) can be expected to feature different degrees of polarization, some assumptions are needed to handle polarization in the retrieval: In the UV, single scattering will be assumed both for the light scattered of the clouds and the background Rayleigh scattering. This is motivated by the efficient absorption of upwelling UV radiation from the lower atmosphere by the stratospheric ozone layer. In the IR, while unpolarised radiation can be assumed from the airglow emission, the background radiation is more complex. Analysis carried out with the SASKTRAN radiative transfer simulator (Bourassa et al., 2008) indicates that the degree of background polarisation will vary from between 0.1 to 0.2 depending on the albedo of the lower atmosphere, which can be estimated from the data obtained by the albedo photometers on MATS.

~~Based on the measurement data in orbit~~In general, ~~the~~ contributions of background and straylight to the total signal can be difficult to distinguish from each other. ~~In addition,~~ This is in part due to the fact that both wanted and unwanted signals ~~can be~~ are expected to vary in similar ways along the orbit. Most notable, upwelling radiation, and thus local conditions at lower altitudes, will affect O_2 Atmospheric Band dayglow, NLC scattering, molecular Rayleigh background, ~~and~~ as well as straylight. In the MATS data processing, the procedures for removing background and straylight are therefore closely linked ~~and will partly rely on the same auxiliary information, e.g. from the IR background channels or the albedo photometers~~.

~~4.3.1 Airglow channels~~

As for the removal of background and straylight from the O_2 Atmospheric Band channels, ~~The~~ the two IR background channels (Table 4) provide the starting point ~~for removing background and straylight in the O_2 Atmospheric Band channels~~. The amplitude of the straylight is estimated from the signals seen in the IR background channels at the highest altitudes, where we expect negligible contribution from other sources of light. The background from the nominal ~~feild~~ field of view, on the other hand, is estimated using the full background channel images. ~~It~~ This compensates not only for the Rayleigh background, but also for the possible presence of NLC, and for other airglow and possibly auroral emission features. ~~However, t~~The total contribution ~~by~~ of these signals cannot be estimated by simple linear interpolation between the two IR background channels. Rather, these signals show distinct spectral dependence (Sheese et al., 2010). In particular, since O_2 resonantly absorbs upwelling radiation in the Atmospheric Band itself, both scattered background and straylight are weaker than what would be expected from linear interpolation between the two background channels. To account for this, the lower atmospheric albedo needs to be quantified, regarding both absolute albedo and relative flux inside and outside the Atmospheric ~~band~~Band, which in turn depends on lower atmospheric cloudiness and cloud top height. This will be monitored by the pair of nadir-looking albedo photometers onboard MATS that measure upwelling radiation inside and outside the Atmospheric Band~~ onboard MATS~~. In combination with radiative transfer simulations of the relevant processes (Bourassa et al., 2008), this provides a more quantitative straylight and background correction, following the method described by Sheese et al. (2010).

~~4.3.2 NLC channels~~

As for the removal of background and straylight from the NLC channels,~~Signals to be removed from the NLC data~~ signals of concern are molecular Rayleigh background and straylight. Because of efficient absorption of UV radiation by stratospheric ozone, the major source for out-of-field straylight is Rayleigh scattering in the upper stratosphere, and the amount depends on the atmospheric ozone abundance and solar position. Similar to the IR, the amplitude of straylight will be estimated by assuming that the signal seen at the highest altitudes in the NLC images is completely dominated by straylight. As an option, Rayleigh background and the straylight will be removed only after the tomography has been completed. This is done to combine information from both spectral channels and from as many images as possible to estimate the Rayleigh scattering and straylight, which can be assumed to vary slowly in the horizontal direction. Atmospheric density profiles from an atmospheric model (NRLMSISE-~~90~~00) will provide an initial estimate of the molecular Rayleigh background in the field of view. This estimate can then further be improved by normalizing it to the scattering observed under cloud-free conditions.

4.4 Tomography

~~4.4.1 Terminology~~

Tomography will be applied on the images to reconstruct three-dimensional fields of atmospheric emission (or scattering).This will be done using an iterative maximum a-posteriori method (MAP) (Rodgers, 2000). Here the 3D field of emission is described by a state vector, x, and the measured limb radiances by the measurement vector, y. These vectors are related via a linear forward model

$$y = K x \tag{1}$$

K is the Jacobian matrix and describes how emissions x from locations throughout the measurement volume contribute to radiances y from individual limb lines of sight. K thus contains the physics of the measurement, including observation geometry, radiative transfer, and instrument characteristics. For the MATS retrieval processing, K will be geometrically calculated on a grid using a spherical (rotating) earth geometry. Absorption by ozone (in the UV channels) and self-absorption (in the Atmospheric Band channels) will be included using a pre-existing climatology to calculate the optical depth along the path.

Assuming that we have some a~~-~~ priori knowledge about the atmospheric emission described by the vector $\hat{x}$ and a covariance matrix S_a, the maximum a~~-~~ posteriori state, x, can be found using Bayesian estimation by solving the equation

$$\hat{x} = (K^T S_e^{-1} K + S_a^{-1})^{-1} K^T S_e^{-1} (y - Kx) \tag{2}$$

where S_e is the covariance matrix for the measurement vector y.

For large scale problems, inverting equation 2 can become extremely memory-intensive to the point where a direct solver based on decomposition no longer is a possibility. Thus, the equation needs to be solved iteratively. Ungermann et al. (2010) have shown that this can be done efficiently by rewriting the equation above as

$$(K^T S_e^{-1} K + S_a^{-1})\hat{x} = K^T S_e^{-1} (y - Kx) \tag{3}$$

and solving it iteratively using the conjugate gradient method.

As Figure 1 illustrates, the MATS observation geometry provides a large number of lines of sight through a given atmospheric volume. However, a challenge for the MATS tomographic retrieval is that lines of sight only span over a limited range of observation angles (6°), and that lines of sight cover very long paths (hundreds of kilometres) through an airglow layer or NLC layer. Tomographic retrievals under these conditions have been discussed by Krisch et al. (2017).

~~4.4.2 Test retrievals of NLCs~~

To illustrate the feasibility of the tomographic reconstruction, a prototype retrieval has been set up using a simple forward model with a pure spherical geometry (non-rotating earth) and ignoring atmospheric absorption. A three-dimensional test field of NLC scattering coefficients is based on a combination of Odin/OSIRIS vertical profiles and AIM/CIPS images, and covers a horizontal area of 5000 km along orbit and ±175 km across track (upper panel in Figure 8). Forward model simulations and retrievals are performed on a set of measurements covering roughly 3000 km along track (containing 167 limb images to be processed), ±125 km on each side of the orbit plane, and altitudes from 60 to 100 km. The resolution of the grid is 20×6.4×0.5 km in the along-track, across-track and vertical direction, respectively. Measurements are simulated with random noise added assuming shot-noise-limited performance with signal to noise ratios defined by the instrument specification. The measurement covariance matrix is set correspondingly (diagonal elements only). The retrievals are performed with very lax constraints using an a -priori atmosphere equal to the background atmosphere and an a-priori covariance matrix with only diagonal entries equal to 10^{-8} m^{-1} sr^{-1}.

The result from this retrieval test is shown in the lower panel of Figure 8. For the area fully covered by MATS measurements, i.e. 2000-3000 km along-track~~ / +-~~ and ±125 km across-track, the retrieval successfully reproduces the atmospheric field. For the area fully covered by the tomography, the mean square error amount to 1.5×10^{-10} m^{-1} sr^{-1}, which corresponds to a relative error of 3% for a typical cloud brightness of 5×10^{-9} m^{-1} sr^{-1}. As expected, some degradation can be seen on the edges due to limited tomographic information, with no information at the outermost regions where no measurement data is available. Along-track these effects will be mitigated by performing the retrieval on subsequently overlapping volumes along the orbit.

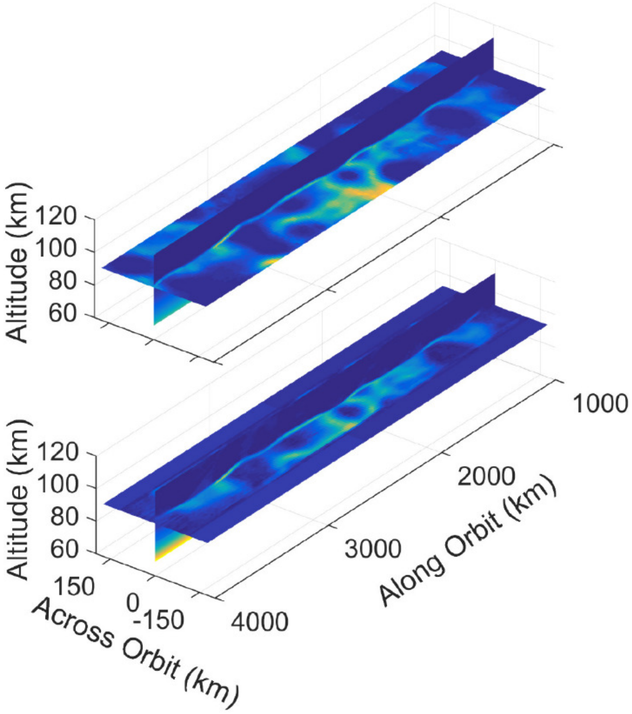

Figure 8. Example of tomographic retrieval simulations. The upper panel shows the simulated "true" NLC volume scattering coefficient. The lower panel shows the retrieved NLC. Based on the simulated lines of sight, full retrieval is available in an area 2000-3000 km along orbit and ±125 km across orbit.

4.5 O_2 Atmospheric Band spectroscopy

Following the tomographic retrieval of volume emission rates, the O_2 Atmospheric Band is analysed to reveal temperature and oxygen densities. Starting point for the temperature retrieval is the ratio, R, of the signals in the two Atmospheric Band channels. Figure 9 shows the (re-)distribution of the rotational transitions in the 0-0 vibrational band as a function of temperature. With a lifetime of 12 s, the rotational distribution of O_2 ($b^1\Sigma$) is in thermodynamic equilibrium up to altitudes around 120 km, and thus representative for atmospheric temperature. The filter curves of the two MATS Atmospheric Band channels ("total" and "centre") have been chosen so that the ratio R provides maximum sensitivity to temperature in the temperature range of interest.

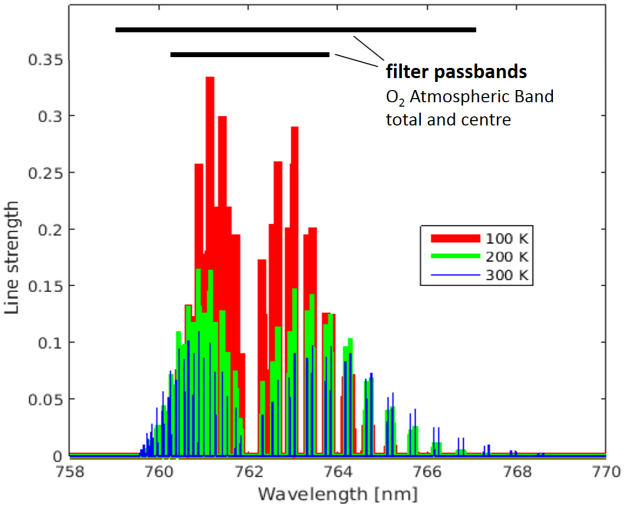

Figure 9. Spectral distribution of the O_2 Atmospheric Band rotational transitions in the 0-0 vibrational band as a function of temperature. The filter passbands of the limb instrument's Atmospheric Band channels cover the total band and its central part, respectively.

Using Gaussian error estimation and assuming the error from each channel is roughly equal, the random error in the retrieved temperature is

$$\Delta T = \sqrt{2}\frac{\Delta\epsilon}{\epsilon}\frac{dT}{dR} \tag{4}$$

where ϵ and $\Delta\epsilon$ are the retrieved volume emission and its RMS error, and dT/dR is the sensitivity of the temperature to the ratio between the signals in the two channels. In order to achieve a temperature precision of 2 K, a signal-to-noise ratio $\epsilon/\Delta\epsilon$ better than 500 is needed, with can typically be achieved between 90 and 100 km altitude during daytime. It should be noted that the RMS error depends not only on the instrument, but also the covariance matrices used in the retrieval. The tomographic retrieval will apply horizontal and vertical regularization to suppress noise in the retrieved field. Hence, based on the true performance of the MATS instrument, further trade-off studies will be made between noise and spatial resolution in terms of measurement integration times, pixel binning, and regularization.

As stated in Table 1, possibilities to spectroscopically retrieve temperature from the O_2 Atmospheric Band nightglow are more limited. When providing temperature data with the maximum tomographic resolution of 60×20×1 km, the precision of at nighttime will be 5-20 K. Again, the temperature precision can be improved by spatial or temporal averaging, at the cost of reduced spatial resolution of the tomographic output. However this trade-off is handled, possibilities to retrieve gravity wave data from the temperature field are rather limited during nighttime. Notwithstanding this limitation of the temperature analysis, nighttime gravity wave data can be obtained directly from the tomographically retrieved spatial distribution of nightglow volume emission rates.

The total volume emission rate of the Atmospheric Band provides direct information about the concentration of excited molecular oxygen O_2 ($b^1\Sigma$). This is also the basis for retrieving concentrations of ozone and atomic oxygen, which are intimately linked to O_2 ($b^1\Sigma$) via dayglow photochemical reactions (Evans et al., 1988). As compared to the more complex daytime retrievals, the Atmospheric Band nightglow emission is largely only dependent on atomic oxygen, which allows for rather direct retrieval of atomic oxygen concentrations (Sheese et al., 2011).

4.6 NLC spectroscopy

The tomographic retrievals from the MATS UV channels provide~~s~~ the amount of scattered sunlight by NLC throughout the 3D retrieval grid. Additional NLC information will be available from the Atmospheric Band background channels, thus providing complementary spectral NLC data in the infrared. The ratio of NLC-scattered sunlight and solar irradiance provides the volume scattering coefficient β in each retrieval pixel.

The amount of light scattered from ice particles depends largely on the ratio between the size of the particle and wavelength of the light. Rayleigh scattering applies to particles much smaller that the wavelength, with the scattering coefficient approximately proportional to λ^{-4}. (Note that even in the Rayleigh limit the exponent is not exactly 4, as spectral dependence of the ice particles' index of refraction causes an additional wavelength-dependence.) For larger particles, interactions with the incoming sunlight get more complicated, and the scattering can be described as Mie scattering for spherical particles, or more complex numerical schemes for non-spherical particles (e.g. Mishchenko and Travis, 1998). Even in these more general cases, the wavelength dependence of the scattering in a limited spectral range can conveniently be described by a dependence $\lambda^{-\alpha}$, where λ is the wavelength, and α a size-dependent exponent, the so-called Ångström exponent (e.g. von Savigny et al., 2005). This Ångström description is frequently used in particle size retrieva~~e~~ls, relating spectral measurements of particle scattering to theoretical descriptions of scattering as a function of particle size. For the two UV channels of the MATS limb instrument, the Ångström exponent is obtained as

$$\alpha = \frac{\log(\lambda_2) - \log(\lambda_1)}{\log(\beta_1) - \log(\beta_2)} \tag{5}$$

Once the Ångström exponent in each tomographic retrieval pixel is determined, this value can be compared to scattering simulations of different ice particle distributions. Figure 11 shows an example of a lookup table connecting particles sizes and Ångström exponent for the MATS UV wavelengths. It is important to note, however, that the information that can be retrieved about the NLC particle population is limited: The Ångström exponent provides a single piece of information, and can thus determine one parameter describing the size distribution, e.g. a mode radius. This makes it necessary to make assumptions about additional parameters describing the particle population. Here we use the same assumptions that have been used in earlier retrieval studies e.g. for the AIM/CIPS or Odin/OSIRIS instrument. This includes oblate spheroid ice particles with an axial ratio~~n~~ of ~~0.5~~2, and a normal distribution of particle sizes with a distribution width that varies with the mode radius (Lumpe et al., 2013; Hultgren and Gumbel, 2014). As Figure 10 shows, the resulting relationship between Ångström coefficient and particle sizes will generally be ambiguous for larger mode radii exceeding about 100 nm. A method to remove this ambiguity is to involve information from the infrared channels in the retrieval (Karlsson and Gumbel, 2004). Physically, NLC particle populations are expected to have mode radii below 100 nm. Once particle size information has been inferred in the form of a mode radius, absolute scattering coefficient and size information can be combined to also retrieve the local ice content (ice mass density) of the cloud.

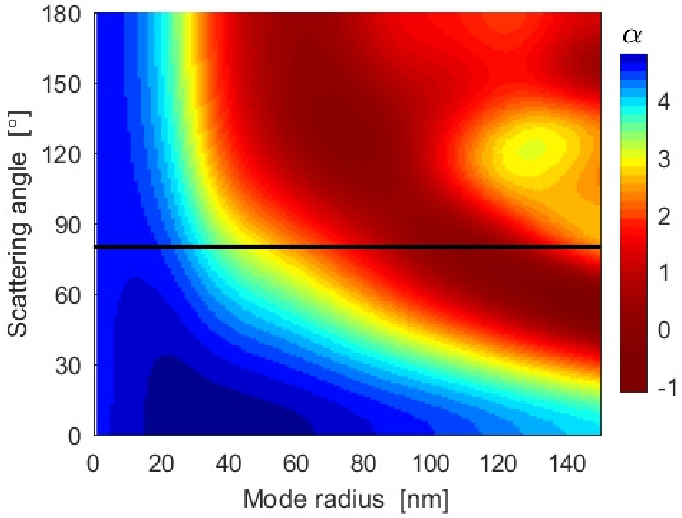

Figure 10. A lookup table for the NLC particle size analysis, generated from T-matrix simulations. Shown is the Ångström exponent as a function of mode radius and scattering angle. The black line indicates a typical scattering angle for MATS NLC observations.

Through Gaussian error propagation the error in the Ångström parameter in a retrieval pixel can be estimated through

$$\Delta\alpha = \frac{\sqrt{2}}{\log(\lambda_1) - \log(\lambda_2)} \frac{\Delta\beta}{\beta} \tag{6}$$

where $\Delta\beta$ is the uncertainty of the retrieved volume scattering coefficient, assuming it is roughly equal for the two wavelengths. From this, the error in the mode radius and ice mass density can be estimated through scattering simulations. In order to achieve a precision of 0.25 in the Ångström exponent, a signal-to-noise ratio $\beta / \Delta\beta$ better than 50 is needed.

4.7 Retrieval of gravity waves

As described in the previous sections, tomographic and spectroscopic analysis will provide three-dimensional fields of airglow emission rate, temperature, oxygen species, and NLC properties. These primary data products have been summarized in Table 1. All of these data fields can serve as input to an analysis of gravity waves and other atmospheric structures. However, there is a particular interest in wave retrievals from the temperature field as it opens for an analysis in terms gravity wave momentum flux (GWMF), potential energy density and other quantitative wave properties (Ern et al, 2004; Fritts et al., 2014). The gravity wave retrieval involves several steps. Starting point is to infer spatial temperature variations, after calculation of a mean background temperature field. The three-dimensional temperature variations are then the basis for identifying horizontal and vertical wavelengths or wave numbers. Subsequent analysis builds on basic wave relationships as described e.g. by Fritts and Alexander (2003). Applying the dispersion relation, intrinsic frequency and group velocity can be inferred from wavenumbers and background temperature. This is the basis for a subsequent retrieval of directional GWMF (Ern et al., 2004; 2011). This also needs (climatological) data on atmospheric density. Retrieval at multiple altitudes allows for an analysis of vertical GWMF gradients, and thus the momentum forcing (wave drag) of the background flow. An important goal is to obtain seasonal and latitudinal climatologies of gravity wave spectra, and to identify the contribution of different wavelengths to GWMF and wave drag. Such an analysis requires knowledge about a sensitivity function, i.e. the response of the MATS wave retrieval in terms of a wave's horizontal and vertical wavelength, and orientation, as well as observation conditions. Detailed descriptions of wave retrievals and sensitivities are beyond the scope of the curremt paper and will be provided in future publications about MATS data products.

~~Since one of the major goals of~~ In order to demonstrate MATS' ~~is~~ ability to reconstruct gravity wave structures, the tomographic method has been ~~also~~ tested on a set of coherent gravity waves observable in the Atmospheric Band emission. The emission field is generated using a simple airglow gravity wave model (Li, 2017). Using the same forward model as for the NLC simulations (Section 4.4), MATS limb instrument images are simulated, and the three-dimensional emission fields are retrieved using the MAP method. 200 images have been simulated, covering 6000 km along-track and 400 km across-track with a resolution of 5×5×0.25 km.

This has been tested for wave structures aligned both along the movement of the satellite, and perpendicular to it. As part of these tests, the horizontal and vertical wavelengths are varied. The amplitude of the retrieved wave is then compared to the amplitude of the true wave field. The ratio between these indicates the contrast in the retrieved data and is referred to as the gravity wave sensitivity for a certain wavelength (Preusse et al., 2002). In Figure 11, the sensitivity is shown for along-track waves, i.e. waves with fronts aligned perpendicular to the satellite track. Gravity waves with horizontal wavelengths down to 60 km and vertical wavelengths down to 3 to 5 km can be detected with a contrast better than 0.8. Also for across-track waves (not shown), vertical wavelengths can be inferred down to 3 km with a strong signal, but horizontal wavelengths can be retrieved down to 20 km, only limited by the resolution of the image. For both along-track and across-track waves, wave structures with vertical wavelength down to 1 km can be detected, albeit with a reduction in amplitude by more than 50 %.

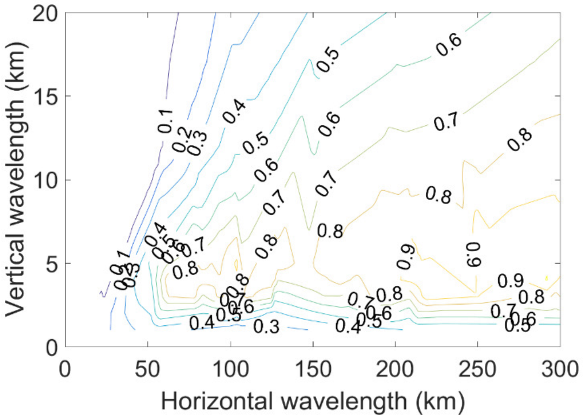

Figure 11. Simulated sensitivity of the MATS instrument to gravity waves of varying horizontal and vertical wavelengths. Results are shown for waves with wave fronts perpendicular to orbit plane. The sensitivity is defined as the ratio between the amplitude of the retrieved wave and the amplitude of the true wave field.

5 Operational Planning

During routine operations, MATS will spend most of the time taking images using nominal science modes defined for the mission. Based on season and time of day, different atmospheric phenomena are to be observed and, hence, different imaging channels will operate. Beyond the nominal science modes, certain measurements must be performed in order to characterize the instrument in orbit. These calibration modes will be carried out with certain intervals, and involve changes in control settings for both the payload and the platform. During normal operations a set of commands will be uploaded once per week. For commands that are required to be executed at a particular point in space, the timing of the commands will use predicted satellite orbits, based on orbit data ("two-line elements") gathered up to two weeks in advance.

5.1 Science modes

When defining operational measurement modes, an important constraint is the total data volume as defined by the satellite's downlink capacity. Hence, compromises must be made concerning image resolution, image compression, sampling interval, geographical coverage, and number of channels in operation. "NLC modes" will be active during the NLC season, i.e. summer months in either hemisphere. During that period, the UV limb channels are given priority to operate at high resolution at summer latitudes poleward of 45°. The resolution of the IR limb channels is kept moderate in order to keep data volumes down. "IR modes" will be active outside the NLC season and involve no data collection in the UV channels, which allows the IR channels to operate at higher resolution. The IR nadir camera will always be operated during nighttime, producing a rather small data volume. Tables 5 and 6 summarize basic instrument settings in NLC and IR modes. The resulting measurements are the basis for the retrieval of the primary data product listed in Table 1.

In addition to the instrument settings in Tables 5 and 6, the platform attitude can be adapted in accordance with specific measurement objectives. A standard viewing geometry is to take subsequent limb images centred around the satellite orbit plane. At the highest latitudes, this provides aligned images as input tomographic retrieval. However, at lower latitudes the Earth rotation leads to a continuous shifting of the atmospheric scene with respect to the orbit plane. ~~Mats~~ MATS provides the option to compensate for this in terms of a continuous yaw movement of the satellite. This movement lets the limb field of view follow the Earth rotation, thus keeping a targeted section of the atmosphere aligned between subsequent limb images.

NLC Mode (May 1 - September 10, November 1 - March 10)							
Channel	UV1	UV2	IR1	IR2	IR3	IR4	Nadir
Horizontal pixel~~-~~ size (km)	5	5	10	10	50	50	10×10
Vertical pixel size (km)	0.2	0.2	0.4	0.4	0.8	0.8	N/A
Number of across-track pixels	50	50	25	25	5	5	18.5
Number of vertical pixels	200	200	138	138	69	69	N/A
Readout interval (s)	3	3	5	5	5	5	~1,4
Integration time (s)	<3	<3	<5	<5	<5	<5	1
JPEG quality (%)	90	90	90	90	90	90	N/A
Data per image (kB)	4.31	4.31	1.49	1.49	0.15	0.15	0.08
Active fraction of orbit (%)	30	30	100	100	100	100	30
Images per orbit	540	540	1080	1080	1080	1080	1157
Data per orbit (kB)	2325	2325	1604	1604	160	160	96

Table 5. Image readout in the six limb channels and the nadir channel during "NLC mode". Information about pixels refers to image pixels that are created from ~~on-chip~~ binning of the individual CCD pixels. The total image data amounts to 8275 kB per orbit.

IR Mode (March 11 - April 30, September 11 - October 31)							
Channel	UV1	UV2	IR1	IR2	IR3	IR4	Nadir
Horizontal pixel~~-~~ size (km)	-	-	5	5	50	50	10×10
Vertical pixel size (km)	-	-	0.4	0.4	0.8	0.8	N/A
Number of across-track pixels	-	-	50	50	5	5	18.5
Number of vertical pixels	-	-	138	138	69	69	N/A
Readout interval (s)	-	-	5	5	5	5	~1,4
Integration time (s)	-	-	<5	<5	<5	<5	1
JPEG quality (%)	-	-	94	94	94	94	N/A
Data per image (kB)	-	-	3.68	3.68	0.18	0.18	0.08
Active fraction of orbit (%)	0	0	100	100	100	100	10
Images per orbit	0	0	1080	1080	1080	1080	386
Data per orbit (kB)	0	0	3972	3972	199	199	32

Table 6. Image readout in the six limb channels and the nadir channel during "IR mode". Information about pixels refers to image pixels that are created from ~~on-chip~~ binning of the individual CCD pixels. The total image data amounts to 8373 kB per orbit.

5.2 Calibration modes

In addition to the above science modes, a number of measurements are to be performed to characterize the instrument in orbit. Calibration measurements will be carried out with certain intervals, and involve changes in control settings for both the payload and the platform. Moreover, special manoeuvres can be performed to verify the integrity of the instrument after launch or at other occasions.

The driver for these calibration and special modes is that instrument properties may change in time, and need to be monitored. Table 7 lists main properties in this regard, including satellite operations and time scales over which changes can occur. These properties may in turn be dependent on operational parameters like solar position, instrument temperature etc., and should be monitored together as a function of those, if applicable. For these characterization activities, dedicated attitude operations have been defined for the platform, e.g. providing pointing towards the lower (Rayleigh-scattering) atmosphere, dark space, the moon or stars. During these measurements the CCDs may be operated with different integration times, with reduced pixel binning or full image readout.

Property	**Satellite operation**	**Timescale**
Dark current	Pointing into darkness.	Weeks
Readout bias	Pointing into darkness.	Months
Bad pixels	Pointing into darkness.	Weeks
Noise level	Pointing into darkness.	Months
Polarization sensitivity	Role motion, pointing to various altitudes.	Years
Stray light	Limb scanning from brighter lower altitudes to darkness.	Years
Point spread function	Pointing at stars.	Years
Relative spectral calibration	Pointing at moon. Pointing to lower altitudes.	Years
Absolute calibration	Pointing to lower atmosphere. Pointing at moon.	Months
Instrument pointing	Pointing at stars.	Months

Table 7. Properties of the MATS limb instrument that need to be characterized during the mission.

6 Outlook

In the late 1950s, Georg Witt laid the foundation for mesospheric research in Sweden. Studying NLC by ground-based photography, he applied stereoscopic analysis to infer three-dimensional structures of the clouds (Witt, 1962). 60 years later, the MATS satellite is about to study three-dimensional structures in the mesosphere by tomographic observations from space. Georg Witt passed away in 2014, but he was still with us when MATS was proposed and selected earlier the same year. His scientific ideas will be with us when MATS flies.

At the time this paper is written, MATS is being prepared for launch in late 2019. Platform, instruments, and system have passed Critical Design Reviews, and are now going through assembly, integration and testing. Pre-flight calibration procedures have been developed and are being applied to characterize instrument properties like sensitivity, spectral and polarisation dependence, dark current and other CCD characteristics. In parallel, procedures and software are being developed for data handling, tomographic and spectroscopic retrieval, and scientific analysis.

Basic measurement targets in the upper mesosphere and lower thermosphere are O_2 Atmospheric Band airglow and NLC. From these, the primary data products emission rate, temperature, atomic oxygen and ozone, as well as NLC brightness and particle size will be retrieved (Table 1). Based on these three-dimensional data products, an analysis in terms of gravity waves and other dynamical structures will be conducted. This needs essentially two steps: firstly, (wave) structures need to be identified, which involves appropriate filtering against noise and small-scale fluctuations; secondly accessible wave parameters like horizontal and vertical wavelengths, wave orientation, and momentum flux will be addressed. The resulting wave climatology can be analysed e.g. in terms of wave spectra, as a function of latitude and season, and in relationship to dynamic conditions and drivers in other parts of the atmosphere. Co-analysis with other missions and meteorological data will be central to these efforts. Modelling efforts will be decisive to combine different parts of these studies into the larger picture of atmospheric dynamics.

At all stages of the above analysis, collaboration with other research groups will be necessary and highly welcome. This concerns both the MATS dynamics objectives and mesospheric cloud objectives as defined in Section 1.1. The launch of the MATS satellite will be followed by an intense period of consolidating observational data and retrieval methods. Initial work on the scientific analysis will then be conducted by a core team of collaborating research groups. This will soon be followed by general releases of data products on the different levels.

As for NLC studies, there will be a natural connection to the Odin satellite mission, providing a comprehensive OSIRIS NLC climatology of 17 years so far (Gumbel and Karlssson, 2011). Beyond climatology, as the orbits of MATS and Odin will be in close proximity, there are also perspectives towards more direct co-analysis on an orbit-to-orbit basis. Based on overlapping orbits, true common-volume NLC studies are envisaged between MATS and AIM/CIPS. This follows the path already laid out by common volume studies between AIM and Odin (Benze et al., 2017; Broman et al., this issue). Joint studies by CIPS and MATS will make use of the complementary nature of the missions with the highly resolved horizontal data of CIPS and the three-dimensional tomographic data of MATS.

An example of a "whole atmosphere" perspective is a collaboration envisaged between MATS and several NASA missions, together providing the potential of gravity wave studies ranging from the troposphere to the thermosphere. Various methods for gravity wave analysis have been developed for AQUA/AIRS from the troposphere to mid-stratosphere (e.g., Gong et al, 2012; Hoffmann et al., 2012), for AIM/CIPS in the stratopause region (Randall et al., 2017), and for the Global-scale Observations of the Limb and Disk (GOLD) in the lower thermosphere (Greer et al., 2018). As a complement to these missions, the MATS gravity wave analysis fills an important gap in the upper mesosphere. As described in the introduction, these perspectives coincide with an era of increasing model abilities to explicitly simulate ~~of~~ gravity waves from tropospheric sources to effects in the middle and upper atmosphere (Watanabe et al., 2015; Becker and Vadas, 2018). An important basis for linking MATS results to the dynamics of the troposphere and stratosphere will also be the co-analysis with meteorological datasets. In particular, high-resolution data from the Integrated Forecasting System (IFS) of the European Centre for Medium-Range Weather Forecasts (ECMWF) have been shown to well reproduce gravity wave activity throughout the stratosphere (Dörnbrack et al., 2017; Ehard et al., 2018).

On a local basis, the three-dimensional MATS data will provide new opportunities for joint studies with ground-based instrumentation. Ground-based networks with focus on wave analysis like the ARISE project will be of particular interest (Blanc et al., 2018). In the field of NLC and related mesospheric ice phenomena, local measurements include lidars and MST radars. In the field of airglow, local measurements include ground-based nightglow imaging and related spectroscopic temperature analysis. Wave studies in the MLT will also benefit from coincident MATS tomography and local time- and altitude-resolved measurements of wind (e.g., by meteor radar) or temperature (e.g. by resonance lidars). On an even more detailed level, co-analysis is possible between three-dimensional MATS data fields and coincident sounding rocket experiments. It is important to note that many of these local studies also provide valuable possibilities to validate MATS measurements and analysis methods. Extending local co-analysis into the thermosphere and ionosphere, the objectives of MATS are closely related to scientific goals of the EISCAT_3D incoherent scatter radar system (Aikio et al., 2014) and similar radar networks. Three-dimensional data fields from both measurement systems can open for intriguing new studies on dynamical structures and coupling processes across the MLT.

Author contribution

JG, LM, OMC, DPM, JS, BK and GW have contributed to the conceptional development of the MATS science mission. LM and OMC have been project leaders for the MATS instrument development; JG, NK and DPM have contributed to the overall coordination of the project. OMC, JD, GG, JG, AH, JH, NI, MK, AL, SM, LM, DPM, GO, JR and JS have worked with the development of instruments, retrieval and scientific analysis. SC, SP, WP and AH have designed the limb telescope. JG, DPM, NI and BK have contributed to the acquisition of financial support for the mission. JG, OMC, LM and NK have prepared the manuscript with contributions from the co-authors.

Competing interests

The authors declare that they have no competing interests.

Acknowledgements

We thank the teams at Omnisys Instruments, OHB-Sweden, and ÅAC Mictrotec. Their dedicated engineering and management work has made the MATS payload and the InnoSat/MATS satellite platform possible. The scientific development of the mission has benefitted greatly from discussions with many scientists. We are particularly grateful to Gerd Baumgarten, Erich Becker, Adam Bourassa, Doug Degenstein, Patrick Eriksson, Manfred Ern, Patrick Espy, Craig Haley, Mark Hervig, Martin Kaufmann, Yvan Orsolini, Kristell Pérot, Dave Rusch, Kaoru Sato, Mike Stevens, Mike Taylor, Christian von Savigny, and Kaley Walker. We thank Andreas Fjeldstad, Björn Linder, Markus Janghede, Franz Kanngieser, Tobias Kuremyr, Daniel Pettersson, Simon Pfreundschuh, Tejaswi Seth, and Sarah Zayouna for their contributions to instrument development, instrument characterization and retrieval development. We thank Susanne Benze, Lina Broman, Koen Hendrickx, Maartje Kuilman, and Marin Stanev for their engagement in the MATS science questions. The MATS project is funded by the Swedish National Space Agency (SNSA), and we especially acknowledge the commitment of their representative Ronnie Lindberg. Additional financial support has been provided by the Erna and Victor Hasselblad Foundation. The development of the off-axis telescope was supported by the National Research Foundation of Korea (grant NRF-2014M1A3A3A02034810, BK21 plus programme).

References

Aikio, A., McCrea, I., and the EISCAT 3D Science Working Groups: EISCAT 3D Science Case, Report for the EISCAT 3D Preparatory Phase Project WP3, 2014.

Akmaev, R. A.: Whole atmosphere modeling: Connecting terrestrial and space weather, Rev. Geophys., 49, RG4004, doi: 10.1029/2011RG000364, 2011.

Alexander, M. J.: Global and seasonal variations in three-dimensional gravity wave momentum flux from satellite limb-sounding temperatures, Geophys. Res. Lett., 42, 6860–6867, doi: 10.1002/2015GL065234, 2015.

Alexander, M. J., et al.: Recent developments in gravity-wave effects in climate models and the global distribution of gravity-wave momentum flux from observations and models, Q. J. R. Meteorol. Soc., 136, 1103-1124, doi:10.1002/qj.637, 2010.

Anderson, D. N.: Modeling the ambient, low latitude F-region ionosphere - a review, J. Atmos. Terr. Phys., 43, 753-762, 1981.

Azeem, I., Yue, J., Hoffmann, L., Miller, S. D., Straka III, W. C., and Crowley, G.: Multisensor profiling of a concentric gravity wave event propagating from the troposphere to the ionosphere, Geophys. Res. Lett., 42, 7874-7880, doi: 10.1002/2015GL065903, 2015.

Babcock, H. D., and Herzberg, L.: Fine structure of the red system of atmospheric oxygen bands, Astrophys. J., 108, 167-190, doi: 10.1086/145062, 1948.

Bailey, S. M., Thomas, G. E., Hervig, M. E., Lumpe, J. D., Randall, C. E., Carstens, J. N., Thurairajah, B., Rusch, D. W., Russell, J. M., and Gordley, L. L.: Comparing nadir and limb viewing observations of polar mesospheric clouds: The effect of the assumed particle size distribution, J. Atmos. Sol. Terr. Phys., 127, 51-65, doi: 10.1016/j.jastp.2015.02.007, 2015.

Becker, E.: Dynamical Control of the Middle Atmosphere, Space Sci. Rev., 168, 283, doi: 10.1007/s11214-011-9841-5, 2012.

Becker, E., and Vadas, S. L.: Secondary gravity waves in the winter mesosphere: Results from a high-resolution global circulation model, J. Geophys. Res., 123, 2605-2627, 2018.

Benze, S., Gumbel, J., Randall, C. E., Karlsson, K., Hultgren, K., Lumpe, J. D., Baumgarten, G.: Making limb and nadir measurements comparable: A common volume study of PMC brightness observed by Odin OSIRIS and AIM CIPS, J. Atmos. Sol. Terr. Phys., 167, 66-73, doi: 10.1016/j.jastp.2017.11.007, 2018.

Blanc, E., Ceranna, L., Hauchecorne, A. et al.: Toward an improved representation of middle atmospheric dynamics thanks to the ARISE project, Surv. Geophys., 39, 171-225, doi: 10.1007/s10712-017-9444-0, 2018.

Bourassa, A., Degenstein, D., and Llewellyn, E. J.: SASKTRAN: A spherical geometry radiative transfer code for efficient estimation of limb scattered sunlight. J. Quant. Spec. Rad. Transf., 107, 52-73, 2008.

Carbary, J. F., Morrison, D., and Romick, G. J.: Transpolar structure of polar mesospheric clouds, J. Geophys. Res., 105, 24763-24769, 2000.

Carlotti, M., Dinelli, B. M., Raspollini, P., and Ridolfi, M.: Geo-fit approach to the analysis of limb-scanning satellite measurements, Appl. Optics, 40, 1872-1885, doi: 10.1364/ORS.2001.OWC5, 2001.

Chandran, A., Rusch, D., Palo, S. E., Thomas, G. E., and Taylor, M.: Gravity wave observatiosn from the Cloud Imaging and Particle Size (CIPS) experiment on the AIM Spacecraft, J. Atmos. Solar-Terr. Phys., doi:10.1016/j.jastp.2008.09.041, 2009.

Chang, S.: Linear astigmatism of confocal off-axis reflective imaging systems with N-conic mirrors and its elimination, J. Opt. Soc. Am. A, 32, 852-859, doi: 10.1364/JOSAA.32.000852, 2015.

Chau, J. L., Goncharenko, L. P., Fejer, B. G., and Liu, H.-L.: Equatorial and low latitude ionospheric effects during sudden stratospheric warming events, Space Sci. Rev., doi:10.1007/ s11214-011-9797-5, 2011.

Chen, P.-R.: Two-day oscillation of the Equatorial Ionization Anomaly, J. Geophys. Res., 97, 6343-6357, 1992.

Christensen O. M., Eriksson, P., Urban, Murtagh, D. P., Hultgren, K., and Gumbel, J.: Tomographic retrieval of water vapour and temperature around polar mesospheric clouds using Odin-SMR, Atmos. Meas. Tech., 8, 1981-1999, doi: 10.5194/amt-8-1981-2015, 2015.

Christensen O. M., Benze, S., Eriksson, P., Gumbel, J., Megner, L., and Murtagh, D. P.: The relationship between polar mesospheric clouds and their background atmosphere as observed by Odin-SMR and Odin-OSIRIS Atmos. Chem. Phys., 16, 12587-12600, doi: 10.5194/acp-16-12587-2016, 2016.

de Wit, R. J., Hibbins, R. E., Espy, P. J., Orsolini, Y. J., Limpasuvan, V., and Kinnison, D. E.: Observations of gravity wave forcing of the mesopause region during the January 2013 major Sudden Stratospheric Warming, Geophys. Res. Lett., 41, 4745-4752, doi: 10.1002/2014GL060501, 2014.

Degenstein, D. A., Llewellyn, E. J., and Lloyd, N. D.: Volume emission rate tomography from a satellite platform, Appl. Opt., 42, 1441-1450, 2003.

Degenstein, D.A., Llewellyn, E. J., and Lloyd, N. D.: Tomographic retrieval of the oxygen infrared atmospheric band with the OSIRIS infrared imager, Can. J. Phys., 82, 501-515, 2004.

Dörnbrack, A., Gisinger, S., Pitts, M. C., Poole, L. R., and Maturilli, M.: Multilevel cloud structure over Svalbard, Mon. Wea. Rev., 145, 1149-1159, doi: 10.1175/MWR-D-16-0214.1, 2017.

Ehard, B., Malardel, S., Dörnbrack, A., Kaifler, B., Kaifler, N., and Wedi, N.: Comparing ECMWF high resolution analyses to 20 lidar temperature measurements in the middle atmosphere. Q. J. R. Met. Soc., 144, 633-640, doi: 10.1002/q j. 3206, 2018.

Ern, M., Preusse, P., Alexander, M. J., and Warner, C. D.: Absolute values of gravity wave momentum flux derived from satellite data, J. Geophys. Res., 109, D20103, doi: 10.1029/2004JD004752, 2004.

Ern, M., P. Preusse, P., Gille, J. C., Hepplewhite, C. L., Mlynczak, M. G., Russell III, J. M., and Riese, M.: Implications for atmospheric dynamics derived from global observations of gravity wave momentum flux in stratosphere and mesosphere, J. Geophys. Res., 116, D19107, doi: 10.1029/2011JD015821, 2011.

Ern, M., Preusse, P., Kalisch, S., Kaufmann, M., and Riese, M.: Role of gravity waves in the forcing of quasi two-day waves in the mesosphere: An observational study, J. Geophys. Res., 118, 3467-3485, doi: 10.1029/2012JD018208, 2013.

Ern, M., Trinh, Q. T., Kaufmann, M., Krisch, I., Preusse, P., Ungermann, J., Zhu, Y., Gille, J. C., Mlynczak, M. G., Russell III, J. M., Schwartz, M. J., and Riese, M.: Satellite observations of middle atmosphere gravity wave absolute momentum flux and of its vertical gradient during recent stratospheric warmings, Atmos. Chem. Phys., 16, 9983-10019, doi: 10.5194/acp-16-9983-2016, 2016.

Ern, M., Hoffmann, L., and Preusse, P.: Directional gravity wave momentum fluxes in the stratosphere derived from high-resolution AIRS temperature data, Geophys. Res. Lett., 44, 475-485, doi: 10.1002/2016GL072007, 2017.

Espy, P. J., Jones, G. O. L., Swenson, G. R., Tang, J., and Taylor, M. J.: Seasonal variations of the gravity wave momentum flux in the Antarctic mesosphere and lower thermosphere, J. Geophys. Res., 109, D23109, doi:10.1029/2003JD004446, 2004.

Evans, W., McDade, I., Yuen, J., and Llewellyn, E.: A rocket measurement of the O_2 infrared atmospheric (0-0) band emission in the dayglow and a determination of the mesospheric ozone and atomic oxygen densities. Can. J. Phys., 66, 941-946, 1988.

Forbes, J. M., and Leveroni, S.: Quasi 16-day oscillation in the ionosphere, Geophys. Res. Lett., 19, 981-984, 1992.

Forbes, J. M., Zhang, X., Palo, S. E., Russell III, J. M., Mertens, C. J., and Mlynczak, M. G., Kelvin waves in stratosphere, mesosphere and lower thermosphere temperatures as observed by TIMED/SABER during 2002-2006, Earth Planets Space, 61, 4, 447-453, 2009.

Forbes, J. M., Bruinsma, S. L., Doornbos, E., and Zhang, X.: Gravity wave-induced variability of the middle thermosphere, J. Geophys. Res. Space Physics, 121, 6914-6923, doi: 10.1002/2016JA022923, 2016.

Fritts, D. C., and Alexander, M. J.: Gravity wave dynamics and effects in the middle atmosphere, Rev. Geophys., 41, 1003, doi: 10.1029/2001RG000106, 2003.

Fritts, D. C., Vadas, S. L., Wan, K., and Werne, J. A.: Mean and variable forcing of the middle atmosphere by gravity waves, J. Atmos Solar-Terr. Phys., 68, 247-265, doi: 10.1016/j.jastp.2005.04.010, 2006.

Fritts, D. C., Pautet, P.-D., Bossert, K., Taylor, M. J., Williams, B. P., Iimura, H., Yuan, T., Mitchell, N. J., and Stober, G.: Quantifying gravity wave momentum fluxes with Mesosphere Temperature Mappers and correlative instrumentation, J. Geophys. Res.-Atmos., 119, 2014JD022150, 13583–13603, doi: 10.1002/2014JD022150, 2014.

Funke, B., López-Puertas, M., Bermejo-Pantaleón, D., García-Comas, M., Stiller, G. P., von Clarmann, T., Kiefer, M., and Linden, A.: Evidence for dynamical coupling from the lower atmosphere to the thermosphere during a major stratospheric warming, Geophys. Res. Lett., 37, L13803, doi: 10.1029/2010GL043619, 2010.

Gao, H., Li, L., Bu, L., Zhang, Q., Tang, Y., and Wang, Z.: Effect of Small-Scale Gravity Waves on Polar Mesospheric Clouds Observed From CIPS/AIM, J. Gophys. Res., 123, 4026-4045, doi: 10.1029/2017JA024855, 2018.

Geller, M. A., Alexander, M. J., Love, P. T., Bacmeister, J., Ern, M., Hertzog, A., Manzini, E., Preusse, P., Sato, K., Scaife, A. A., and Zhou, T.: A comparison between gravity wave momentum fluxes in observations and climate models, J. Clim., 26, 6383-6405, 2013.

Giono, G., Olentšenko, G., Ivchenko, N., Christensen, O. M., Gumbel, J., Frisk, U., Hammar, A., Davies, I., Megner, L., and the MATS team: Characterisation of the analogue read-out chain for the CCDs onboard the Mesospheric Airglow/Aerosol Tomography and Spectroscopy (MATS), Proc. SPIE, 10698, 1-8, doi: 10.1117/12.2313732, 2018.

Gong, J., Wu, D. L., and Eckermann, S. D.: Gravity wave variances and propagation derived from AIRS radiances, Atmos. Chem. Phys., 12, 1701-1720, doi: 10.5194/acp-12-1701-2012, 2012.

Greer, K. R., England, S. L., Becker, E., Rusch, D., and Eastes, R.: Modeled gravity wave-like perturbations in the brightness of far ultraviolet emissions for the GOLD mission, J. Geophys. Res., 123, 5821-5830. doi: 10.1029/2018JA025501, 2018.

Gumbel, J., and Karlsson, B.: Intra- and inter-hemispheric coupling effects on the polar summer mesosphere, Geophys. Res. Lett., 38, L14804, doi: 10.1029/2011GL047968, 2011.

Hammar, A., Christensen, O. M., Park, W., Pak, S., Emrich, A., and Stake, J.: Stray light suppression of a compact off-axis telescope for a satellite-borne instrument for atmospheric research, Proc. SPIE 10815, Optical Design and Testing VIII, 108150F, doi: 10.1117/12.2500555~~accepted for publication in Proc. SPIE/COS~~, 2018.

Hammar, A., Park, W., Chang, S., Pak, S., Emrich, A., and Stake, J.: Wide-field off-axis telescope for the Mesospheric Airglow/Aerosol Tomography Spectroscopy satellite, Appl. Opt. 58, 1393-1399, doi: 10.1364/AO.58.001393, 2019.

Hart, V. P., Taylor, M. J., Doyle, T. E., Zhao, Y., Pautet, P.-D., Carruth, B. L., Rusch, D. W., and Russell, J. M.: Investigating gravity waves in polar mesospheric clouds using tomographic reconstructions of AIM satellite imagery, J. Geophys. Res., 123, 955-973, doi: 10.1002/2017JA024481, 2018.

Hoffmann, L., and Alexander, M. J.: Retrieval of stratospheric temperatures from Atmospheric Infrared Sounder radiance measurements for gravity wave studies, J. Geophys. Res., 114, D07105, doi: 10.1029/2008JD011241, 2009.

Holton, J. R.: The role of gravity wave induced drag and diffusion in the momentum budget of the mesosphere, J. Atmos. Sci., 39, 791-799, doi: 10.1175/1520-0469, 1982.

Holton, J. R.: The generation of mesospheric planetary waves by zonally asymmetric gravity wave breaking. J. Atmos. Sci., 41, 3427-3430, doi: 10.1175/1520-0469, 1984.

Hultgren, K., and Gumbel, J.: Tomographic and spectral views on the lifecycle of polar mesospheric clouds from Odin/OSIRIS, J. Geophys. Res., 119, 14129-14143, doi: 10.1002/2014JD022435, 2014.

Hultgren, K., Gumbel, J., Degenstein, D., Bourassa, A., Lloyd, N. D., and Stegman, J.: First simultaneous retrievals of horizontal and vertical structures of Polar Mesospheric Clouds from Odin/OSIRIS tomography, J. Atmos. Solar-Terr. Phys., 104, 213-223, 2013.

Kaifler, N., Kaifler, B., Wilms, H., Rapp, M., Stober, G., and Jacobi, C.: Mesospheric temperature during the extreme midlatitude noctilucent cloud event on 18/19 July 2016. J. Geophys. Res., 123, 13775–13789, doi: 10.1029/2018JD029717, 2018.

Kalisch, S., Preusse, P., Ern, M., Eckermann, S. D., and Riese, M.: Differences in gravity wave drag between realistic oblique and assumed vertical propagation, J. Geophys. Res. Atmos., 119, 10,081-10,099, doi: 10.1002/2014JD021779, 2014.

Karlsson, B., and Gumbel, J.: Challenges in the limb retrieval of noctilucent cloud properties from Odin/OSIRIS, Adv. Space Res., 36, 935-942, 2005.

Karlsson, B., and ~~Theodore G.~~ Shepherd, T. G.: The improbable clouds at the edge of the atmosphere, Physics Today, 71, 6, 30-36, doi: 10.1063/PT.3.3946, 2018.

Kaufmann, M., Blank, J., Guggenmoser, T., Ungermann, J., Engel, A., Ern, M., Friedl-Vallon, F., Gerber, D., Grooß, J. U., Guenther, G., Höpfner, M., Kleinert, A., Kretschmer, E., Latzko, Th., Maucher, G., Neubert, T., Nordmeyer, H., Oelhaf, H., Olschewski, F., Orphal, J., Preusse, P., Schlager, H., Schneider, H., Schuettemeyer, D., Stroh, F., Suminska-Ebersoldt, O., Vogel, B., M. Volk, C., Woiwode, W., and Riese, M.: Retrieval of threedimensional small-scale structures in upper-tropospheric/lower-stratospheric composition as measured by GLORIA, Atmos. Meas. Tech., 8, 81-95, doi: 10.5194/amt-8-81-2015, 2015.

Körnich, H., and Becker, E.: A simple model for the interhemispheric coupling of the middle atmosphere circulation, Adv. Space Res., 45, 661-668, doi:10.1016/j.asr.2009.11.001, 2010.

Krebsbach, M., and Preusse, P.: Spectral analysis of gravity wave activity in SABER temperature data, Geophys. Res. Lett., 34, L03814, doi: 10.1029/2006GL028040, 2007.

Krisch, I., Ungermann, J., Preusse, P., Kretschmer, E., and Riese, M.: Limited angle tomography of mesoscale gravity waves by the infrared limb-sounder GLORIA, Atmos. Meas. Tech., 11, 4327-4344, doi: 10.5194/amt-11-4327-2018, 2018.

Larsson, N., Lilja, R., Gumbel, J., Christensen, O. M., and Örth, M.: The MATS micro satellite mission − tomographic perspective on the mesosphere, ESA Proceedings of the 4s Symposium, Valletta, Malta, May 2016, pp. 11070-11078, 2016.

Li, A.: A 3D-model for O_2 airglow perturbations induced by gravity waves in the upper mesosphere, M.Sc. thesis, Chalmers University of Technology, 2017.

Limpasuvan, V., Wu, D. L., Schwartz, M. J., Waters, J. W., Wu, Q., and Killeen, T. L.: The two-day wave in EOS MLS temperature and wind measurements during 2004–2005 winter, Geophys. Res. Lett., 32, L17809, doi: 10.1029/2005GL023396, 2005.

Lindzen, R. S.: Turbulence and stress owing to gravity wave and tidal breakdown, J. Geophys. Res., 86, 9707, doi: 10.1029/JC086iC10p09707, 1981.

Liu, H.-L., Marsh, D. R., She, C.-Y., Wu, Q., and Xu, J.: Momentum balance and gravity wave forcing in the mesosphere and lower thermosphere, Geophys. Res. Lett., 36, doi: 10.1029/2009GL037252, 2009.

Liu,X., Yue, J., Xu, J., Wang, L., Yuan, W., Russell III, J. M., and Hervig, M. E.: Gravity wave variations in the polar stratosphere and mesosphere from SOFIE/AIM temperature observations, J. Geophys. Res., 119, 7368-7381, doi: 10.1002/2013JD021439, 2014.

Livesey, N. J., Van Snyder, W., Read, W. G., and Wagner, P. A.: Retrieval algorithms for the EOS microwave limb sounder (MLS), IEEE Trans. Geosci. Rem. Sens., 44, 1144-1155, 2006.

Llewellyn, E. J., Lloyd, N. D., Degenstein, D. A., Gattinger, R. L., Petelina, S. V., Bourassa, A. E., Wiensz, J. T., Ivanov, E. V., McDade, I. C., Solheim, B. H., McConnell, J. C., Haley, C. S., von Savigny, C., Sioris, C. E., McLinden, C. A., Griffioen, E., Kaminski, J., Evans, W. F. J., Puckrin, E., Strong, K., Wehrle, V., Hum, R. H., Kendall, D. J. W., Matsushita, J., Murtagh, D. P., Brohede, S., Stegman, J., Witt, G., Barnes, G., Payne, W. F., Piché, L., Smith, K., Warshaw. G., Deslauniers, D.-L., Marchand, P., Richardson, E. H., King, R. A., Wevers, I., McCreath, W., Kyrölä, E., Oikarinen, L., Leppelmeier, G. W., Auvinen, H., Mégie, G., Hauchecorne, A., Lefèvre, F., de La Nöe, J., Ricaud, P., Frisk, U., Sjöberg, F., von Schéele, F., and Nordh, L.: The OSIRIS instrument on the Odin spacecraft, Can. J. Phys., 82, 411-422, doi: 10.1139/p04-005, 2004.

Marks, C. J., and Eckermann, S. D.: A three-dimensional nonhydrostatic ray-tracing model for gravity waves: Formulation and preliminary results for the middle atmosphere, J. Atmos. Sci., 52, 1959-1984, 1995.

Marsh, D. R., Garcia, R. R., Kinnison, D. E., Boville, B. A., Sassi, F., Solomon, S. C., and Mathes, K.: Modeling the whole atmosphere response to solar cycle changes in radiative and geomagnetic forcing, J. Geophys. Res., 112, D23306, doi: 10.1029/2006JD008306, 2007.

McDade, I., Murtagh, D., Greer, R., Dickinson, P., Witt, G., Stegman, J., Llewellyn, E., Thomas, L., and Jenkins, D.: ETON 2: Quenching parameters for the proposed precursors of O_2 ($b^1\Sigma_g^+$) and O (^1S) in the terrestrial nightglow, Planet. Space Sci., 34, 789-800, doi: 10.1016/0032-0633(86)90075-9, 1986.

McLandress, C., Shepherd, T. G., Polavarapu, S., and Beagley, S. R.: Is missing orographic gravity wave drag near 60°S the cause of the stratospheric zonal wind biases in chemistry-climate models?, J. Atmos. Sci., 69, 802-818, doi: 10.1175/JAS-D-11-0159.1, 2012.

Megner, L., Christensen O. M., Karlsson, B., Benze, S., and Fomichev,V.: Comparison of retrieved noctilucent cloud particle properties from Odin tomography scans and model simulations, Atmos. Chem. Phys., 16, 15135-15146, doi: 10.5194/acp-16-15135-2016, 2016.

Megner, L., Stegman, J., Pautet, P.-D., and Taylor, M. J.: First observed temporal development of a noctilucent cloud ice void. Geophysical Res. Lett., 45. doi: 10.1029/2018GL078501, 2018.

Miller, S. D., Straka III, W. C., Yue, J., Smith, S. M., Alexander, M. J., Hoffmann, L., Setvák, M., and Partain, P. T.: Upper atmospheric gravity wave details revealed in nightglow satellite imagery, Proc. Nat. Acad. Sci., 112, E6728–E6735, doi: 10.1073/pnas.1508084112, 2015.

Mishchenko, M. I., and Travis, L. D.: Capabilities and limitations of a current FORTRAN implementation of the T-matrix method for randomly oriented, rotationally symmetric scatterers, J. Quant. Spectrosc. Radiat. Transfer, 60, 309-324, doi: 10.1016/S0022-4073(98)00008-9, 1998.

Mlynczak, M. G., Morgan, F., Yee, J.-H., Espy, P., Murtagh, D., Marshall, B., and Schmidlin, F.: Simultaneous Measurements of the O_2 ($^1\Delta$) and O_2 ($^1\Sigma$) airglows and ozone in the daytime mesosphere, Geophys. Res. Lett., 28, 999-1002, 2001.

Murtagh, D. P., Witt, G., Stegman, J., McDade, I. C., Llewellyn, E. J., Harris, F., and Greer, R. G. H.: An assessment of proposed O(^1S) and O_2($b^1\Sigma_g^+$) nightglow excitation parameters, Planet. Space Sci., 38, 1, 45-53, 1990.

Murtagh, D., Frisk, U.~~-~~, Merino, F., Ridal, M., Jonsson, A., Stegman, J., Witt, G., Eriksson, P., Jiménez, C., Megie, G., de la Noë, J., Ricaud, P., Baron, P., Pardo, J. R., Hauchcorne, A., Llewellyn, E. J., Degenstein, D. A., Gattinger, R. L., Lloyd, N. D., Evans, W. F. J., McDade, I. C., Haley, C. S., Sioris, C., von Savigny, C., Solheim, B.H., McConnell, J. C., Strong, K., Richardson, E. H., Leppelmeier, G. W., Kyrölä, E., Auvinen, H., Oikarinen, L.: An overview of the Odin atmospheric mission, Can. J. Phys., 80, 309-319, 2002.

Oberheide, J., Forbes, J. M., Häusler, K., Wu, Q., and Bruinsma, S. L.: Tropospheric tides from 80 to 400 km: Propagation, interannual variability, and solar cycle effects, J. Geophys. Res., 114, D00I05, doi: 10.1029/2009JD012388, 2009.

Park, J., Lühr, H., Lee, C., Kim, Y. H., Jee, G., and Kim, J.-H.: A climatology of medium-scale gravity wave activity in the midlatitude/low-latitude daytime upper thermosphere as observed by CHAMP, J. Geophys. Res. Space Physics, 119, 2187-2196, doi: 10.1002/2013JA019705, 2014.

Perwitasari, S., Sakanoi, T., Nakamura, T., Ejiri, M. K., Tsutsumi, M., Tomikawa, Y., Otsuka, Y., Yamazaki, A., and Saito, A.: Three years of concentric gravity wave variability in the mesopause as observed by IMAP/VISI, Geophys. Res. Lett., 43, 11,528–11,535, doi: 10.1002/2016GL071511, 2016.

Plumb, R. A.: Baroclinic instability of the summer mesosphere: a mechanism for the quasi-two-day wave?, J. Atmos. Sci., 40, 262-270, 1982.

Preusse, P., Dörnbrack, A., Eckermann, S. D., Riese, M., Schaeler, B., Bacmeister, J. T., Broutman, D., and Grossmann, K. U.: Space-based measurements of stratospheric mountain waves by CRISTA, 1. Sensitivity, analysis method, and a case study, J. Geophys. Res., 107, 8178, doi: 10.1029/2001JD000699, 2002.

Preusse, P., Eckermann, S. D., and Ern, M.: Transparency of the atmosphere to short horizontal wavelength gravity waves, J. Geophys. Res., 113, D24104, doi: 10.1029/2007JD009682, 2008.

Preusse, P., Eckermann, S. D., Ern, M., Oberheide, J., Picard, R. H., Roble, R. G., Riese, M., Russell III, J. M., and Mlynczak, M. G.: Global ray tracing simulations of the SABER gravity wave climatology, J. Geophys. Res., 114, D08126, doi: 10.1029/2008JD011214, 2009.

Randall, C. E., Carstens, J., France, J. A., Harvey, V. L., Hoffmann, L., Bailey, S. M., Alexander, M. J., Lumpe, J. D., Yue, J., Thurairajah, B., Siskind, D. E., Zhao, Y., Taylor, M. J., and Russell III, J. M.: New AIM/CIPS global observations of gravity waves near 50-55 km, Geophys. Res. Lett., 44, 7044–7052, doi: 10.1002/2017GL073943, 2017.

Rapp, M., and Thomas, G. E.: Modeling the microphysics of mesospheric ice particles: Assessment of current capabilities and basic sensitivities, J. Atmos. Sol. Terr. Phys., 68, 715-744, 2006.

Rapp, M., Lübken, F.-J., Müllemann, A., Thomas, G. E., and Jensen, E. J.: Small-scale temperature variations in the vicinity of NLC: Experimental and model results, J. Geophys. Res., 107 (D19), 4392, doi: 10.1029/2001JD001241, 2002.

Roble, R. G.: On the feasibility of developing a global atmospheric model extending from the ground to the exosphere, in Atmospheric Science Across the Stratopause, Geophys. Monogr. Ser., vol. 123, edited by D. E. Siskind, S. D. Eckermann, and M. E. Summers, pp. 53-67, AGU, Washington, D.C., 2000.

Rodgers, C. D.: Inverse methods for atmospheric sounding: theory and practice, World Scientific, River Edge, N. J., 2000.

Rong, P., Yue, J., Russell III, J. M., Siskind, D. E., and Randall, C. E.: Universal power law of the gravity wave manifestation in the AIM CIPS polar mesospheric cloud images, Atmos. Chem. Phys., 18, 883-899, doi: 10.5194/acp-18-883-2018, 2018.

Röttger, J.: Travelling disturbances in the equatorial ionosphere and their association with penetrative cumulus convection, J. Atmos. Terr. Phys., 39, 987-998, 1977.

Rusch, D. W., Thomas, G. E., McClintock, W., Merkel, A.W., Bailey, S.M., Russell J.M., III, Randall, C. E., Jeppesen, C., Callan, M.: The Cloud Imaging and Particle Size Experiment on the Aeronomy of Ice in the Mesosphere mission: Cloud morphology for the northern 2007 season, J. Atmos. Solar-Terr. Phys., 71, 356-364, 2008.

Sato, K., Watanabe, S., Kawatani, Y., Tomikawa, Y., Miyazaki, K., and Takahashi, M.: On the origins of mesospheric gravity waves, Geophys. Res. Lett., 36, L19801, doi: 10.1029/2009GL039908, 2009.

Sato, K., and Nomoto, M.: Gravity-wave induced anomalous potential vorticity gradient generating planetary waves in the winter mesosphere, J. Atmos. Sci., 72, 3609-3624, doi: 10.1175/JAS-D-15-0046.1, 2015.

Schmidt, T., Alexander, P., and de la Torre , A.: Stratospheric gravity wave momentum flux from radio occultations, J. Geophys. Res. Atmos., 121, 4443-4467, doi: 10.1002/2015JD024135, 2016.

Sheese, P. E., Llewellyn, E. J., Gattinger, R. L., Bourassa, A. E., Degenstein, D. A., Lloyd, N. D., and McDade, I. C.: Temperatures in the upper mesosphere and lower thermosphere from OSIRIS observations of O_2 A-band emission spectra, Can. J. Phys., 88, 919-925, doi: 10.1139/P10-093, 2010.

Sheese, P., McDade, I. C., Gattinger, R. L., and Llewellyn, E. J.: Atomic oxygen densities retrieved from optical spectrograph and infrared imaging system observations of O_2 A-band airglow emission in the mesosphere and lower thermosphere. J. Geophys. Res., 116, D01303, doi: 10.1029/2010JD014640, 2011.

Siskind, D. E., Drob, D. P., Emmert, J. T., Stevens, M. H., Sheese, P. E., Llewellyn, E. J., Hervig, M. E., Niciejewski, R., and Kochenash, A. J.: Linkages between the cold summer mesopause and thermospheric zonal mean circulation, Geophys. Res. Lett., 39, L01804, doi: 10.1029/2011GL050196, 2012.

Steck, T., Höpfner, M., von Clarmann, T., and Grabowski, U.: Tomographic retrieval of atmospheric parameters from infrared limb emission observations, Appl. Opt., 44, 3291-3301, 2005.

Taylor, M. J., Pendleton Jr., W. R., Clark, S., Takahashi, H., Gobbi, D., and Goldberg, R. A.: Image measurements of short-period gravity waves at equatorial latitudes, J. Geophys. Res., 102, 26283-26299, doi: 10.1029/96JD03515, 1997.

Thomas, G. E.: Mesopheric clouds and the physics of the mesopause region, Rev. Geophys., 29, 553-575, 1991.

Thurairajah, B., Bailey, S. M., Cullens, C. Y., Hervig, M. E., and Russell III, J. M.: Gravity wave activity during recent stratospheric sudden warming events from SOFIE temperature measurements, J. Geophys. Res. Atmos., 119, 8091-8103, doi: 10.1002/2014JD021763, 2014.

Trinh, Q. T., Ern, M., Doornbos, E., Preusse, P., and Riese, M.: Satellite observations of middle atmosphere-thermosphere vertical coupling by gravity waves, Ann. Geophys., 36, 425-444, doi: 10.5194/angeo-36-425-2018, 2018.

Ungermann, J., Hoffmann, L., Preusse, P., Kaufmann, M., and Riese, M.: Tomographic retrieval approach for mesoscale gravity wave observations by the PREMIER Infrared Limb-Sounder, Atmos. Meas. Tech., 3, 339-354, 2010.

Ungermann, J., Blank, J., Lotz, J., Leppkes, K., Hoffmann, L., Guggenmoser, T., Kaufmann, M., Preusse, P., Naumann, U., and Riese, M.: A 3-D tomographic retrieval approach with advection compensation for the air-borne limb-imager GLORIA, Atmos. Meas. Tech., 4, 2509-2529, doi: 10.5194/amt-4-2509-2011, 2011.

Vadas, S. L., and Liu, H.-L.: Numerical modeling of the large-scale neutral and plasma responses to the body forces created by the dissipation of gravity waves from 6 h of deep convection in Brazil, J. Geophys. Res., 118, 2593–2617, doi:10.1002/jgra.50249, 2013.

Vadas, S. L., Fritts, D. C., and Alexander, M. J.: Mechanisms for the generation of secondary waves in wave breaking regions. J. Atmos. Sci., 60, 194-214. doi: 10.1029/2004JD005574, 2003.

von Savigny, C., Petelina, B. Karlsson, S. V., Llewellyn, E. J., Degenstein, D. A., Lloyd, N. D., and Burrows, J. P.: Vertical variation of NLC particle sizes retrieved from Odin/OSIRIS limb scattering observations, Geophys. Res. Lett., 32, L07806, doi: 10.1029/2004GL021982, 2005.

von Savigny, C., Robert, C., Bovensmann, H., Burrows, J. P., and Schwartz, M.: Satellite observations of the quasi 5-day wave in noctilucent clouds and mesopause temperatures, Geophys. Res. Lett., 34, L24808, doi: 10.1029/2007GL030987, 2007.

Wang, L., and Alexander, M. J.: Global estimates of gravity wave parameters from GPS radio occultation temperature data, J. Geophys. Res., 115, D21122, doi: 10.1029/2010JD013860, 2010.

Witt, G.: Height, structure and displacements of noctilucent clouds, Tellus, 14, 1-18, 1962.

Wright, C. J., Hindley, N. P., Hoffmann, L., Alexander, M. J., and Mitchell, N. J.: Exploring gravity wave characteristics in 3-D using a novel S-transform technique: AIRS/Aqua measurements over the Southern Andes and Drake Passage, Atmos. Chem. Phys., 17, 8553-8575, doi: 10.5194/acp-17-8553-2017, 2017.

Wu, D. L., Schwartz, M. J., Waters, J. W., Limpasuvan, V., Wu, Q., and Killeen, T. L.: Mesospheric doppler wind measurements from Aura Microwave Limb Sounder (MLS), Adv. Space Res., 42, 7, 1246-1252, doi:10.1016/j.asr.2007.06.014, 2008.

Yue, J., Miller, S. D., Hoffmann, L., and Straka III, W.C.: Stratospheric and Mesospheric concentric gravity waves over Tropical Cyclone Mahasen: joint AIRS and VIIRS satellite observations, J. Atmos. Solar-Terr. Phys., 119, 83-90, 2014.